Earth System Model Aerosol-Cloud Diagnostics Package (ESMAC Diags) Version 1: Assessing E3SM Aerosol Predictions Using Aircraft, Ship, and Surface Measurements

Shuaiqi Tang[1], Jerome D. Fast[1], Kai Zhang[1], Joseph C. Hardin[2], Adam C. Varble[1], John E. Shilling[1], Fan Mei[1], Maria A. Zawadowicz[3] and Po-Lun Ma[1]

[1]Pacific Northwest National Laboratory, Richland, WA, USA
[2]ClimateAI Inc, San Francisco, CA, USA
[3]Brookhaven National Laboratory, Upton, NY, USA

Correspondence to: Shuaiqi Tang (shuaiqi.tang@pnnl.gov)

Abstract. An Earth System Model (ESM) aerosol-cloud diagnostics package is developed to facilitate the routine evaluation of aerosols, clouds and aerosol-cloud interactions simulated by the Department of Energy's (DOE) Energy Exascale Earth System Model (E3SM). The first version focuses on comparing simulated aerosol properties with aircraft, ship, and surface measurements, most of them are measured in-situ. The diagnostics currently covers six field campaigns in four geographical regions: Eastern North Atlantic (ENA), Central U.S. (CUS), Northeastern Pacific (NEP) and Southern Ocean (SO). These regions produce frequent liquid or mixed-phase clouds with extensive measurements available from the Atmospheric Radiation Measurement (ARM) program and other agencies. Various types of diagnostics and metrics are performed for aerosol number, size distribution, chemical composition, CCN concentration and various meteorological quantities to assess how well E3SM represents observed aerosol properties across spatial scales. Overall, E3SM qualitatively reproduces the observed aerosol number concentration, size distribution and chemical composition reasonably well, but overestimates Aitken mode and underestimates accumulation mode aerosols over the CUS and ENA regions, suggesting that processes related to particle growth or coagulation might be too weak in the model. The current version of E3SM struggles to reproduce new particle formation events frequently observed over both the CUS and ENA regions, indicating missing processes in current parameterizations. The diagnostics package is coded and organized in a way that can be easily extended to other field campaign datasets and adapted to higher-resolution model simulations. Future releases will include comprehensive cloud and aerosol-cloud interaction diagnostics.

1. Introduction

Aerosol number, mass, size, composition, and mixing state affect how aerosol populations scatter and absorb solar radiation and influence cloud albedo, amount, lifetime, and precipitation (Twomey, 1977; Albrecht, 1989) by acting as cloud condensation nuclei (CCN) (e.g., Petters and Kreidenweis, 2007). However, there are still knowledge and measurement gaps on the physical and chemical mechanisms regulating the sources, sinks, gas-to-particle partitioning (e.g., secondary formation processes), and spatiotemporal distribution of aerosol populations. Consequently, the representation of the aerosol lifecycle and the interaction of aerosol populations with clouds and radiation in Earth system models (ESMs) still suffer from large uncertainties (Seinfeld et al., 2016; Carslaw et al., 2018), which impacts the ability of ESMs to predict the evolution of the climate system (IPCC, 2013).

To facilitate model evaluation and document the performance of parameterizations in ESMs, many modeling centers have developed standardized diagnostics packages. Some examples focus on meteorological metrics include the U.S. National Center of Atmospheric Research (NCAR) Atmospheric Model Working Group (AMWG) diagnostics package (AMWG, 2021), the U.S. Department of Energy (DOE) Energy Exascale Earth System Model (E3SM, Golaz et al., 2019) diagnostics (E3SM, 2021), the European Union (EU) Earth System Model Evaluation Tool (ESMValTool, Eyring et al., 2016), and the Program for Climate Model Diagnosis and Intercomparison (PCMDI) Metric Package (PMP, Gleckler et al., 2016). Some recent efforts focus on process-oriented diagnostics (POD) that are designed to provide insights into parameterization developments to address long-standing model biases. Maloney et al. (2019) summarizes the activities by the U.S. National Oceanic and Atmospheric Administration (NOAA) Modeling, Analysis, Prediction, and Projections program (MAPP) Model Diagnostics Task Force (MDTF) to apply community-developed PODs to climate and weather prediction models. Zhang et al. (2020) developed a diagnostics package that utilizes statistics derived from long-term ground-based measurements from the DOE Atmospheric Radiation Measurement (ARM) User Facility for climate model evaluation. Aerosol properties, however, are not included in these diagnostics packages.

The international collaborative AeroCom project (Myhre et al., 2013; Schulz et al., 2006) focuses on evaluation of aerosol predictions using available measurements and includes intercomparisons among global models to assess uncertainties in seasonal and regional variations in aerosol properties and their potential impact on climate. Their diagnostics heavily rely on satellite remote sensing products (e.g., aerosol optical depth) which have global coverage but poor spatial and temporal resolution that hinders a process-level understanding of the sources of model uncertainty. More recently, the Global Aerosol Synthesis and Science Project (GASSP, Reddington et al., 2017; Watson-Parris et al., 2019) has developed a global database of aerosol observations from fixed surface sites as well as ship and aircraft

64   platforms from 86 field campaigns between 1990 and 2015 that can be used for model evaluation. Recent

65   field campaigns after year 2015 are not included in this effort.

66   Many aerosol properties are difficult to measure directly. Remote sensing instruments (e.g., ground

67   and satellite radiometers) that only measure radiative properties of column-integrated aerosols, such as

68   optical depth, are frequently used to evaluate model predictions. Instruments such as ground lidars (e.g.,

69   Campbell et al., 2002) or lidars onboard aircraft (e.g., Müller et al., 2014) and satellite (e.g., CALIPSO,

70   Winker et al., 2009) platforms can provide vertical profiles of aerosol extinction, backscatter, and/or

71   depolarization, but they do not directly measure aerosol number, size and composition. Therefore, the

72   quantities measured by remote sensing instruments cannot be used alone to assess model predictions of

73   aerosol-radiation-cloud-precipitation interactions. Surface monitoring sites provide long-term in situ

74   aerosol property measurements but are limited to land locations with far fewer operational sites compared

75   to those dedicated to routine meteorological sampling. Ship and aircraft platforms are commonly

76   deployed during field campaigns to obtain in situ and remote sensing aerosol property measurements in

77   remote or poorly sampled locations such as over the ocean and within the free troposphere, which are

78   highly valuable when studying spatial variations of aerosols. Aircraft platforms also provide a means to

79   obtain coincident measurements of aerosol and cloud properties needed to understand their interactions.

80   Although in-situ ship and airborne aerosol measurements are usually limited to specific locations for short

81   time periods, the increasing number of completed field campaigns conducted over a range of atmospheric

82   conditions provides an opportunity to use them for model evaluation.

83   As noted by Reddington et al. (2017), the considerable investment in collecting field campaign

84   measurements of aerosol properties is underexploited by the climate modeling community. This can be

85   largely attributed to datasets located in disparate repositories and the lack of a standardized file format

86   that requires excessive time and effort spent on manipulating the datasets to facilitate comparisons

87   between observed and simulated values, especially for those unfamiliar with measurement techniques,

88   assumptions, and uncertainties. With many field campaigns conducted since 2015 being available but

89   rarely used for model evaluation, this study describes the first version of the ESM Aerosol-Cloud

90   Diagnostics (ESMAC Diags) package to facilitate the evaluation of ESM-predicted aerosols, utilizing

91   recent measurements from aircraft, ship and surface platforms collected by the U.S. DOE ARM and

92   National Science Foundation (NSF) NCAR user facilities, most of which are in-situ measurements. The

93   overall structure of ESMAC Diags is designed similar to the Aerosol Modeling Testbed for the Weather

94   Research and Forecasting (WRF) model described in Fast et al. (2011), except that ESMAC Diags uses

95   Python to interface the measurements with ESM output and does not preprocess the observational dataset

96   into a common format. The diagnostics package is firstly designed with and applied to E3SM Atmosphere

97   Model version 1 (EAMv1, Rasch et al., 2019). EAMv1 uses an improved modal aerosol treatment

98   implemented based on the 4-mode version of the modal aerosol module (MAM4, Liu et al., 2016), such

99   as improved treatment of H_2SO_4 vapor for new particle formation (NPF), improved secondary organic

100   aerosol (SOA) treatment, new marine organic aerosol (MOA) species, improvements to aerosol

101   convective transport, wet removal, resuspension from evaporation and aerosol-affected cloud

102   microphysical processes (Wang et al., 2020). Only minimal modifications to the diagnostics package are

103   needed for potential application to other ESMs.

104

105   **2.   Introduction of ESMAC Diags**

106   The workflow of ESMAC Diags v1 is illustrated in Figure 1. Most field campaign datasets are directly

107   read by the diagnostics package. In some field campaigns, more than one instrument is used to measure

108   aerosol size distribution over different size ranges. We therefore merge these datasets to create a more

109   complete description of the size distribution. These data are introduced in Section 2.1. Model outputs are

110   extracted at the ground sites and along the flight tracks or ship tracks. The simulation and preprocessing

111   details are provided in Section 2.2. ESMAC Diags reads in these field campaign and model data with

112   quality controls and generates a set of diagnostics and metrics listed in Section 2.3. The diagnostics

113   package is designed to be flexible so that additional measurements and functionality can be included in

114   the future. Figure 2 depicts the directory structure to illustrate the organization of the datasets and code. It

115   is relatively straightforward to add other field campaigns or datasets using this structure. Most of the

116   datasets used in ESMAC Diags are in a standardized netCDF format (NETCDF, 2021); however, some

117   ARM aircraft measurements use different ASCII formats. Currently, the diagnostic package reads

118   observational data directly from their original format. In the long term, we may standardize the

119   observational data format in a similar manner as was done in GASSP project (Reddington et al., 2017).

120

121

122
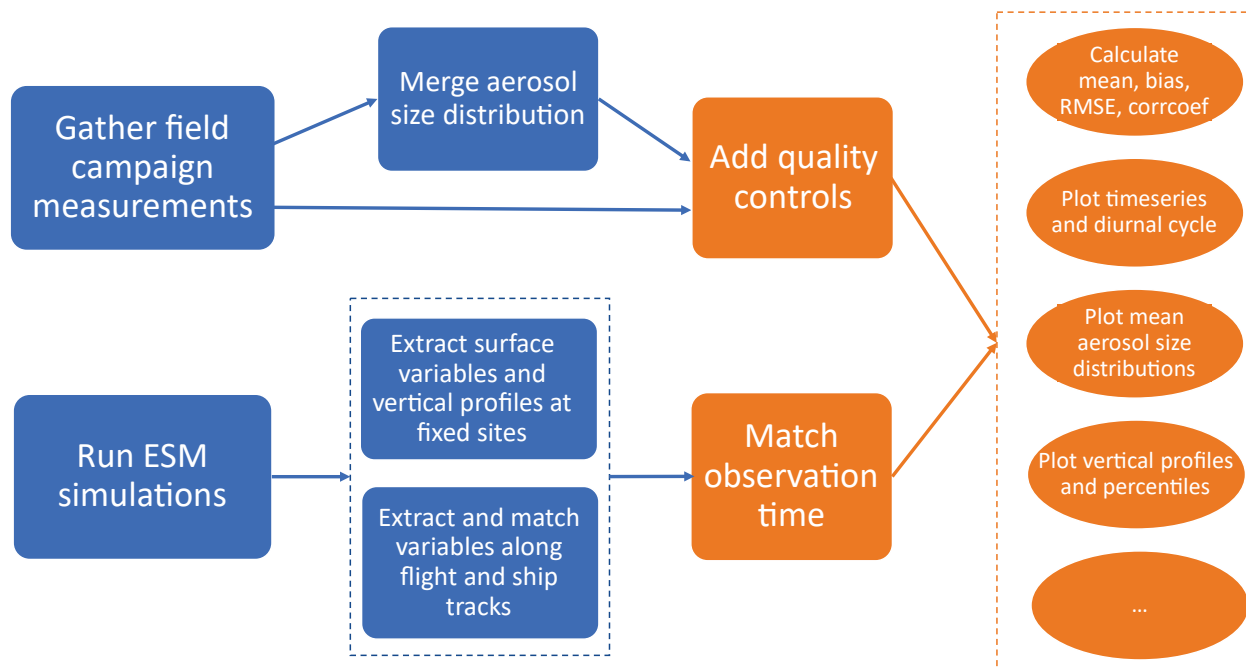
Figure 1: Workflow of ESMAC Diags. Data preprocessing and input are indicated by blue;

123

diagnostics and plotting are indicated by orange.

124

125

126
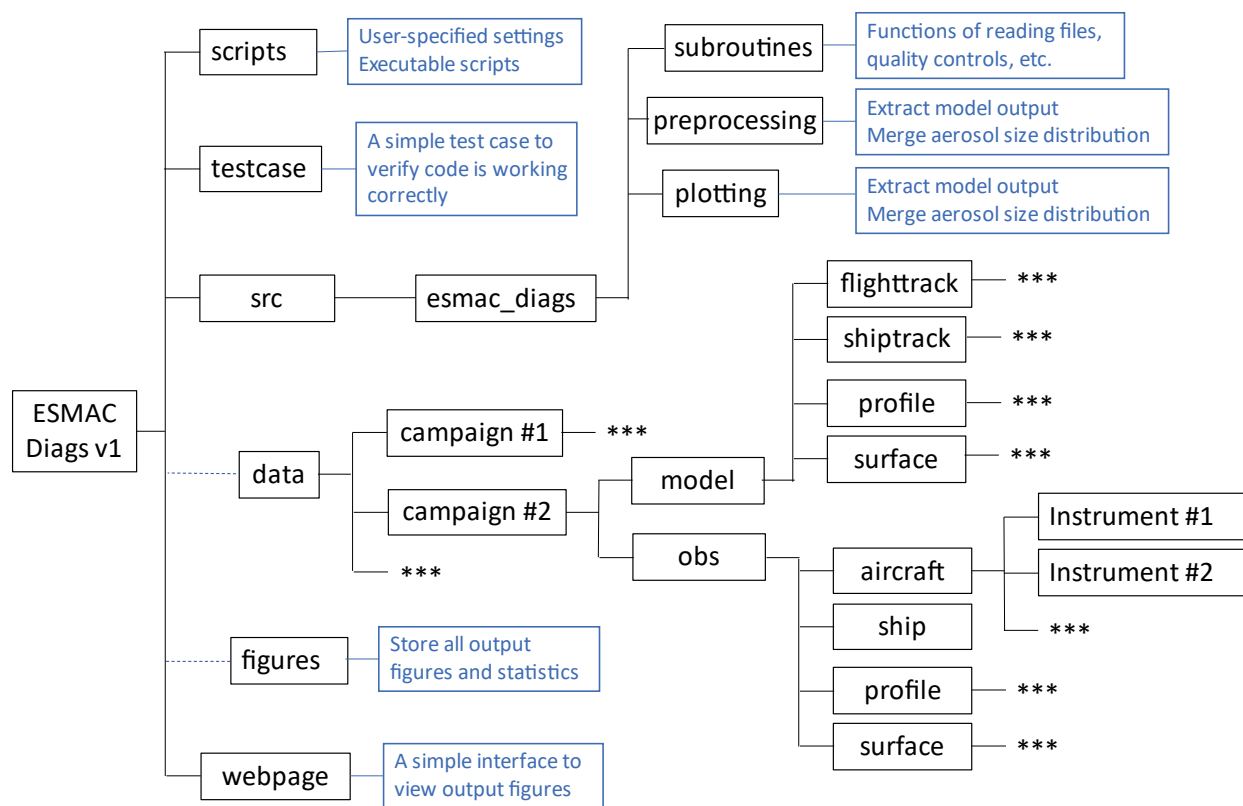
Figure 2: Structure of ESMAC Diags. The "scripts" directory contains executable scripts and user-
specified settings. The "src" directory contains all source code including code used to preprocess
model output, read files, merge measurements from different instruments, compute observed
versus simulated statistical relationships, and plot results. All observational and model data in the
"data" directory are organized by field campaign. The diagnostic plots and statistics are put in the
"figures" directory, also organized by field campaign. The "testcase" directory includes a small
amount of input and verify data to test if the package is installed properly. The "webpage"
directory provides an interface to view diagnostics figures. Boxes in blue describe the functions of
the directory. Asterisks represent boxes that follow the same format as those shown in parallel.

2.1 Field observations and merged aerosol size distribution

We initially focus on four geographical regions where liquid clouds occur frequently and extensive
measurements are available from ARM and other agencies: Eastern North Atlantic (ENA), Northeastern
Pacific (NEP), Central U.S. (CUS, where the ARM Southern Great Plains, SGP, site is located), and
Southern Ocean (SO). Aerosol properties also vary among these regions. Six field campaigns from these
four testbeds are selected in the version 1 of ESMAC Diags (Table 1). HI-SCALE and ACE-ENA are

142   based on long-term ARM ground sites with aircraft field campaigns sampling below, within, and above

143   convective and marine boundary layer clouds, respectively, within a few hundred kilometers around the

144   sites. CSET and MAGIC are field campaigns with aircraft and ship platforms, respectively, sampling

145   transects between California and Hawaii characterized by a transition between stratocumulus and trade

146   cumulus dominated regions. SOCRATES and MARCUS are field campaigns with aircraft and ship

147   platforms, respectively, based out of Hobart, Australia. Aircraft transects during SOCRATES extended

148   south to around 60°S, while ship transects during MARCUS extended southwest from Hobart to

149   Antarctica. The aircraft (black) and ship (red) tracks for these field campaigns are shown in Figure 3.

150   **Table 1. Descriptions of the field campaigns used in this study. Numbers after aircraft or ship**

151   **represent number of flights or ship trips in each field campaign or IOP.**

Campaign*	Period	Platform	Typical Conditions	Reference
HI-SCALE	IOP1: 24 Apr – 21 May 2016 IOP2: 28 Aug – 24 Sep 2016	Ground, aircraft (IOP1: 17, IOP2: 21)	Continental cumulus with high aerosol loading	(Fast et al., 2019)
ACE-ENA	IOP1: 21 Jun – 20 Jul 2017 IOP2: 15 Jan – 18 Feb 2018	Ground, aircraft (IOP1: 20, IOP2: 19)	Marine stratocumulus with low aerosol loading	(Wang et al., 2021)
MAGIC	Oct 2012 – Sep 2013	Ship (18)	Marine stratocumulus to cumulus transition with low aerosol loading	(Lewis and Teixeira, 2015; Zhou et al., 2015)
CSET	1 Jul – 15 Aug 2015	Aircraft (16)	Same as above	(Albrecht et al., 2019)
MARCUS	Oct 2017 – Apr 2018	Ship (4)	Marine liquid and mixed phase clouds with low aerosol loading	(McFarquhar et al., 2021)
SOCRATES	15 Jan – 24 Feb, 2018	Aircraft (14)	Same as above	(McFarquhar et al., 2021)

152   * Full names of the listed field campaigns:
153   HI-SCALE: Holistic Interactions of Shallow Clouds, Aerosols and Land Ecosystems
154   ACE-ENA: Aerosol and Cloud Experiments in the Eastern North Atlantic
155   MAGIC: Marine ARM GCSS Pacific Cross-section Intercomparison (GPCI) Investigation of Clouds
156   CSET: Cloud System Evolution in the Trades
157   MARCUS: Measurements of Aerosols, Radiation and Clouds over the Southern Ocean
158   SOCRATES: Southern Ocean Cloud Radiation and Aerosol Transport Experimental Study
159
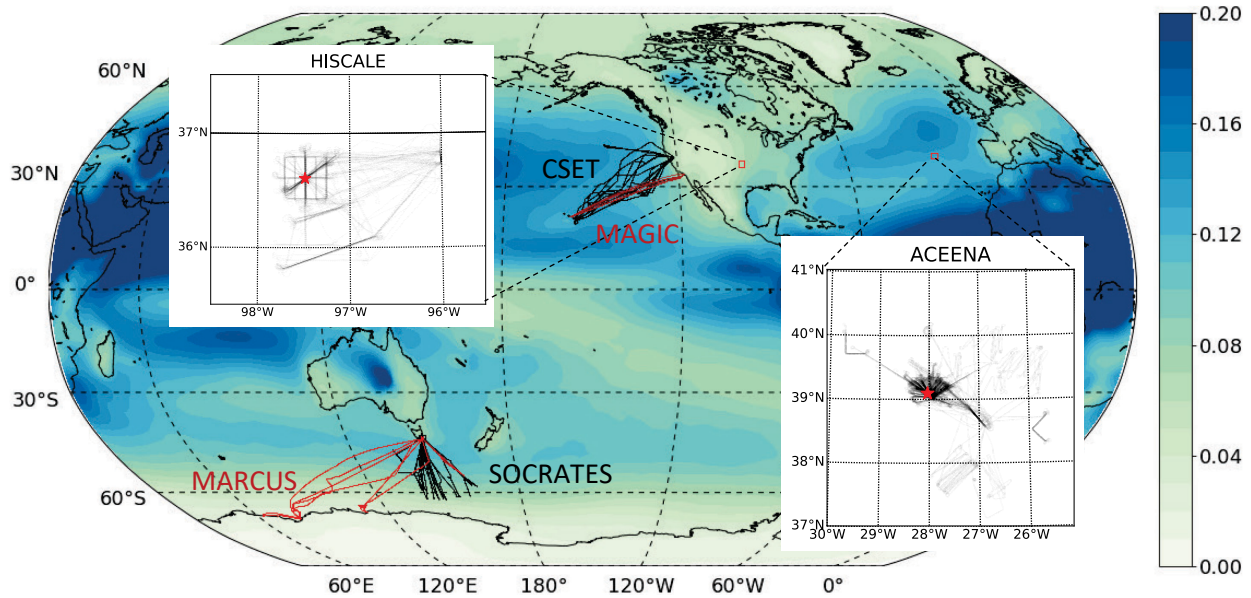
Figure 3. Aircraft (black) and ship (red) tracks for the six field campaigns. Overlaid is aerosol optical depth at 550nm averaged from 2014 to 2018 simulated in EAMv1.

The instruments and measurements used in ESMAC Diags version 1 are listed in Table 2. Note that some instruments are only available for certain field campaigns or failed operationally during certain periods, so that model evaluation is limited by the availability of data collected in each field campaign. ARM data usually include quality flags indicating bad or indeterminate data. These flagged data are filtered out, except surface condensation particle counter (CPC) measurements for HI-SCALE, that data flagged as greater than maximum value (8000 cm^{-3}) are retained since aerosol loading can be higher than that during NPF events. This exception ensures a reasonable diurnal cycle shown in Section 3.3. For some data that do not have a quality flag, a simple minimum and maximum threshold is applied (e.g., 500 cm^{-3} maximum threshold is used for each UHSAS bin from the NCAR research flight measurements).

Table 2. List of instruments and measurements used in ESMAC Diags v1.

Instrument	Platform	Measurements	Available campaigns	DOIs or References
Surface meteorological station (MET)	Ground, ship	Temperature, relative humidity, wind, pressure	HI-SCALE, ACE-ENA, MAGIC, MARCUS	HI-SCALE, ACE-ENA: (Kyrouac and Shi, 2018) MAGIC: (ARM, 2014) MARCUS: 10.5439/1593144
Scanning mobility particle sizer (SMPS)	Ground	Aerosol size distribution (20-700 nm)	HI-SCALE	(Howie and Kuang, 2016)
Nano scanning mobility particle sizer (nanoSMPS)	Ground	Aerosol size distribution (2-150 nm)	HI-SCALE	(Koontz and Kuang, 2016)

Ultra-High Sensitivity Aerosol Spectrometer (UHSAS)	Ground, aircraft, ship	Aerosol size distribution (60 – 1000 nm), number concentration	HI-SCALE, ACE-ENA, MAGIC, MARCUS, CSET, SOCRATES	HI-SCALE, MAGIC, MARCUS: (Koontz and Uin, 2018) ACE-ENA: (Uin et al., 2018) CSET: 10.5065/D65Q4T96 SOCRATES: 10.5065/D6M32TM9
Condensation particle counter (CPC)	Ground, aircraft, ship	Aerosol number concentration (> 10 nm)	HI-SCALE, ACE-ENA, MAGIC, MARCUS	HI-SCALE (ground): (Kuang et al., 2016) ACE-ENA (ground), MAGIC: (Kuang et al., 2018a) MARCUS: (Kuang et al., 2018b) HI-SCALE (aircraft): (ARM, 2016b) ACE-ENA (aircraft): (Mei, 2018)
Condensation particle counter – ultrafine (CPCU)	Ground, aircraft	Aerosol number concentration (> 3 nm)	HI-SCALE, ACE-ENA	HI-SCALE (ground): 10.5439/1046186 HI-SCALE (aircraft): (ARM, 2016b) ACE-ENA (aircraft): 10.5439/1440985
Condensation nuclei counter (CNC)	Aircraft	Aerosol number concentration (11-3000 nm)	CSET, SOCRATES	CSET: 10.5065/D65Q4T96 SOCRATES: 10.5065/D6M32TM9
Cloud condensation nuclei (CCN) counter	Ground, aircraft, ship	CCN number concentration (0.1% to 0.5% supersaturation* depending on the platform)	HI-SCALE, ACE-ENA, MAGIC, MARCUS, SOCRATES	HI-SCALE (ground), ACE-ENA (ground), MARCUS: 10.5439/1342133 MAGIC: 10.5439/1227964 SOCRATES: 10.5065/D6Z036XB HI-SCALE (aircraft): (ARM, 2016a)
Aerosol chemical speciation monitor (ACSM)	Ground	Aerosol composition	HI-SCALE, ACE-ENA	10.5439/1762267
Microwave radiometer (MWR)	Ground, ship	Liquid water path, precipitable water vapor	MAGIC, MARCUS	10.5439/1027369
Counterflow virtual impactor (CVI)	Aircraft	Separates large droplets or ice crystals	HI-SCALE, ACE-ENA, SOCRATES	HI-SCALE: (ARM, 2016a) ACE-ENA: 10.5439/1406248 SOCRATES: 10.5065/D6M32TM9
Fast integrated mobility spectrometer (FIMS)	Aircraft	Aerosol size distribution (10 – 425 nm)	HI-SCALE, ACE-ENA	HI-SCALE: (ARM, 2017) ACE-ENA: (ARM, 2020)
Passive cavity aerosol spectrometer (PCA SP)	Aircraft	Aerosol size distribution (120 – 3000 nm)	HI-SCALE, ACE-ENA, CSET	HI-SCALE: (ARM, 2016a) ACE-ENA: (ARM, 2018) CSET: 10.5065/D65Q4T96
Optical particle counter (OPC)	Aircraft	Aerosol size distribution (390 – 15960 nm)	ACE-ENA	(ARM, 2018)
Interagency working group for	Aircraft	Navigation information and	HI-SCALE, ACE-ENA	HI-SCALE: (ARM, 2017) ACE-ENA: (ARM, 2018)

airborne data and telemetry systems (IWG)		atmospheric state parameters		
High-resolution time-of-flight aerosol mass spectrometer (AMS)	Aircraft	Aerosol composition	HI-SCALE, ACE-ENA	HI-SCALE: (ARM, 2017) ACE-ENA: 10.5439/1468474
Water content measuring system (WCM)	Aircraft	Cloud liquid and total water content	HI-SCALE, ACE-ENA	HI-SCALE: (ARM, 2016a) ACE-ENA: 10.5439/1465759
Doppler lidar (DL)	Ground	Boundary layer height	HI-SCALE	10.5439/1726254
Reprocessed CN and CCN data to remove ship exhaust influence	Ship	CN, CCN number concentration	MARCUS	10.25919/ezp0-em87

174 * For measured supersaturations (SS) that vary over time, a ± 0.05% window is applied (e.g., 0.5% SS

175 includes samples with SS between 0.45% and 0.55%).

176

177 For some field campaigns (HI-SCALE and ACE-ENA), there are several instruments (e.g., FIMS,

178 PCASP, OPC for aircraft; SMPS and nanoSMPS for ground) measuring aerosol size distribution over

179 different size ranges. These datasets are merged to create a more complete size distribution. In ESMAC

180 Diags v1, aerosol "size" refers to mobility and optical dry diameter of particles. The aerosol

181 concentrations in the "overlapping" bins measured by multiple instruments are weighted by the

182 uncertainty of each instrument based on the knowledge of the ARM instrument mentors. An example of

183 the merged aerosol size distribution and individual measurements for one flight in ACE-ENA is shown in

184 Figure 4. Ranging from 10^1 to 10^4 nm, the merged aerosol size distribution data account for ultrafine,

185 Aitken, and accumulation modes.

186 Although these measurements are considered as "truth" when evaluating ESMs, we note that they are

187 subject to limitations and uncertainties due to theoretical/methodological formulations, sampling

188 representativeness, instrumental accuracy and precision, imperfect calibration, random errors, etc. In

189 addition, sampling volumes differ between observations and model output and are not reconcilable. It is

190 difficult to quantify every aspect of observational uncertainty within the context of interpreting

191 comparisons with model output, but we try to discuss some of them in this study to the best of our

192 knowledge. Percentiles (either 25% - 75% or 5% - 95%) are used in some analyses of this study to

193 approximate data variability that is likely to be much higher than measurement uncertainty.
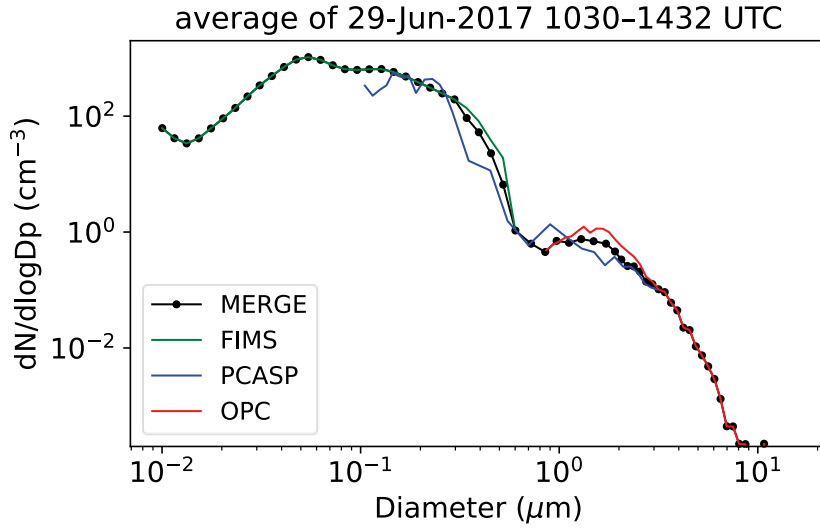
Figure 4. An example of a mean aerosol number distribution merged from FIMS, PCASP and OPC instruments for ACE-ENA aircraft measurements on 29 June 2017.

2.2 Preprocessing of model output

We configured the EAMv1 to follow the Atmospheric Model Intercomparison Project (AMIP) protocol (Gates et al., 1999) with real-world forcings (e.g., greenhouse gases, sea surface temperature, aerosol emissions, etc.). In this study, we run the model from 2012 to 2018, covering all six field campaign periods introduced previously, with enough time for model spin-up. For each simulation year, we use the year 2014 emission data from CMIP6, since the emission data does not cover years after 2014. The simulated horizontal winds are nudged towards the Modern-Era Retrospective analysis for Research and Applications, Version 2 (MERRA-2, Gelaro et al., 2017) with a relaxation time scale of 6 hours. Previous studies (Sun et al., 2019; Zhang et al., 2014) showed that with such nudging configuration the large-scale circulation is well constrained in the nudged simulation, especially for the mid- and high- latitude regions. The simulation uses a horizontal grid spacing of ~1° (NE30, the number of elements along a cube face of the E3SM High-Order Methods Modeling Environment, HOMME, dynamics core) with a 30-minute timestep. We saved hourly output to compare with field campaign measurements. The diagnostics package post-processes 3-D model variables associated with aerosol concentration, size, composition, optical properties, precursor concentration, CCN concentration, and atmospheric state variables. The size of output data is reduced by saving 3-D variables only over the field campaign regions. Appendix A gives the namelist containing variables and regions of E3SM output used in this study. Users can apply it in their own E3SM simulations (or output similar variables if running other models) to use this package.

216   We extracted model output along the aircraft (ship) tracks using an "aircraft simulator" (Fast et al.,
217   2011) strategy to facilitate comparisons of observations and model predictions. At each aircraft (ship)
218   measurement time, we find the nearest model grid cell, output time slice, and vertical level of the aircraft
219   altitude (or the lowest level for ship) to obtain the appropriate model values. Since there are both spatial
220   and temporal mismatch existing between model output and field measurements, the evaluation focuses on
221   overall statistics. We also calculate the aerosol size distribution from 1 nm to 3000 nm at 1 nm increments
222   from the individual size distribution modes in MAM4 to facilitate comparisons with observed aerosol
223   number distribution that has different size ranges for different instruments. All these variables are saved
224   in separate directories according to the specific aircraft (ship) tracks, as indicated in Figure 2.

225   **2.3 List of diagnostics and metrics**

226   Currently, ESMAC Diags produces the following diagnostics and metrics:

227   - Mean value, bias, root mean square error (RMSE) and correlation of aerosol number
228   concentration.
229   - Timeseries of aerosol variables (aerosol number concentration, aerosol number size distribution,
230   chemical composition, CCN number concentration) for each field campaign or intensive
231   observational period (IOP) at the surface or along each flight (ship) track.
232   - Diurnal cycle of aerosol variables at the surface.
233   - Mean aerosol number size distribution for each field campaign or IOP.
234   - Percentiles of aerosol variables by height for each field campaign or IOP.
235   - Percentiles of aerosol variables by latitude for each field campaign or IOP.
236   - Pie/bar charts of observed and predicted aerosol composition averaged over each field campaign
237   or IOP.
238   - Vertical profile of cloud fraction and LWC composite of aircraft measurements for each field
239   campaign or IOP.
240   - Timeseries of atmospheric state variables.
241   - Aircraft and ship track maps.
242

243   In the next section we will demonstrate these diagnostics and metrics by providing several examples.

244

245   **3. Examples**

246 Aerosol number concentration, size distribution, and chemical composition (that controls hygroscopicity)
247 are key quantities that impact aerosol-cloud interactions, such as the activation of cloud droplets. Errors in
248 model predictions of these aerosol properties contribute to uncertainties in aerosol direct and indirect
249 radiative forcing. These aerosol properties vary dramatically depending on location, altitude, season, and
250 meteorological conditions due to variability in emissions, formation mechanisms, and removal processes
251 in the atmosphere. This section shows some examples to illustrate the usage of this diagnostics package
252 on evaluating global models.

253 **3.1 Aerosol size distributions and number concentrations**

254 Aerosol properties are highly dependent on location and season. Figure 5 shows the mean aerosol size
255 distribution for each of the four testbed regions. For HI-SCALE and ACE-ENA, the two IOPs operated in
256 different seasons are shown separately. Table 3 shows the mean aerosol number concentration from these
257 field campaigns, for two particle size ranges: >10 nm and >100 nm. The 25% and 75% percentiles are
258 also shown to illustrate the variability in space and time. Among the four testbed regions, the CUS region
259 has the largest aerosol number concentrations since the other field campaigns are primarily over open
260 ocean. Overall, EAMv1 overestimates Aitken mode (10 – 70 nm) aerosols and underestimates
261 accumulation mode (70 – 400 nm) aerosols for the CUS and ENA regions, suggesting that processes
262 related to particle growth or coagulation might be too weak in the model. Over the NEP region, EAMv1
263 overestimates aerosol number for particle sizes >100 nm and >10 nm (Table 3), both at the surface and
264 aloft. Over the SO region, which is considered a pristine region with low aerosol concentration,
265 observations show a significant number of particles <200 nm in both aircraft and ship measurements
266 (Figure 5). The mean aerosol number concentration over SO region is comparable or even greater than the
267 other ocean testbeds (Table 3). In contrast, EAMv1 simulates a clean environment with the lowest aerosol
268 number concentrations among the four regions. These types of comparisons demonstrate the need for
269 additional analyses to understand why SO has similar aerosol number with other ocean regions and why
270 EAMv1 cannot simulate this feature. The observed 75% percentiles are sometimes smaller than the mean
271 value (Table 3), indicating skewed aerosol size distribution with long tail in large aerosol size. EAMv1
272 usually produces smaller range between 25% and 75% percentiles than the observations, likely because
273 the current model resolution is too coarse to capture the observed spatial variability in aerosol properties.

274

275
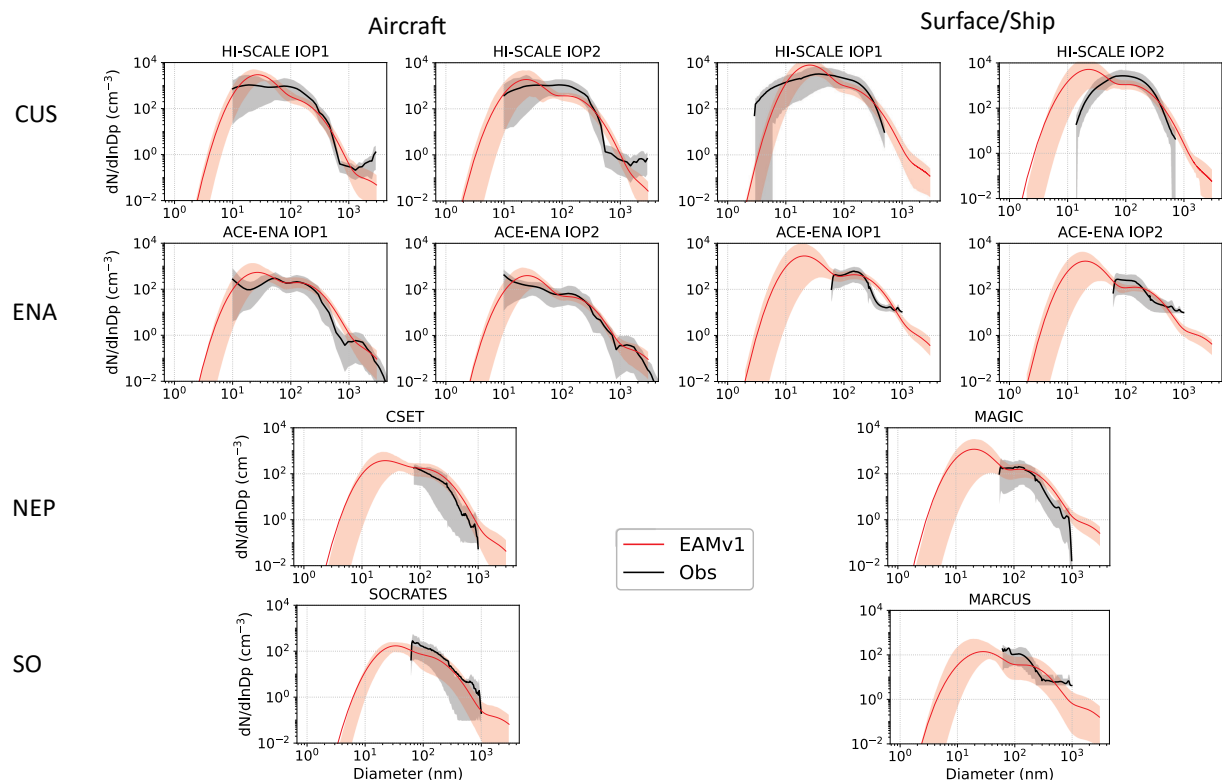
Figure 5: Mean aerosol number distribution averaged for each field campaign or IOP. Shadings denote the range between 10% and 90% percentiles.

278

Table 3: Mean aerosol number concentration and 25% and 75% percentiles (small numbers in parenthesis) for two size ranges averaged for each field campaign (or each IOP for HI-SCALE and ACE-ENA). Aircraft measurements 30 minutes after take-off and before landing are excluded to remove possible contamination from the airport.

Unit: #/cm³			>10 nm		>100 nm	
			CPC	E3SMv1	UHSAS/PCASP*	E3SMv1
CUS	Surface (HI-SCALE)	IOP1	4095 (2198, 4943)	4566 (2865, 5984)	675.1 (393.2, 929.5)	321.3 (229.7, 400.8)
		IOP2	N/A	N/A	N/A	N/A
	Aircraft (HI-SCALE)	IOP1	4206 (1132, 5013)	3872 (2803, 4946)	465.7 (112.6, 616.1)	159.6 (112.2, 200.5)
		IOP2	4121 (1610, 3829)	2514 (1332, 3584)	789.1 (444.4, 1088.0)	383.6 (280.7, 483.8)
ENA	Surface	IOP1	610 (343, 711)	1723 (600, 1650)	206.1 (134.5, 267.1)	209.8 (155.3, 255.5)

	(ACE-ENA)	IOP2	458 (239, 505)	843 (320, 1152)	59.6 (25.0, 71.9)	61.9 (53.6, 71.9)
	Aircraft (ACE-ENA)	IOP1	576 (264, 677)	919 (562, 917)	135.6 (65.3, 185.1)	199.9 (146.6, 266.3)
		IOP2	356 (132, 383)	521 (279, 627)	72.8 (22.2, 72.8)	50.3 (41.6, 62.3)
NEP	Ship (MAGIC)		417 (117, 285)	1271 (356, 1652)	113.6 (47.0, 139.9)	143.0 (93.7, 148.5)
	Aircraft (CSET)		408 (155, 386)	607 (353, 675)	81.5 (17.0, 73.4)	134.5 (81.2, 151.3)
SO	Ship (MARCUS)		354 (244, 415)	303 (164, 326)	68.5 (36.8, 94.0)	54.5 (32.5, 71.7)
	Aircraft (SOCRATES)		988 (327, 991)	237 (169, 270)	56.2 (14.1, 50.4)	32.3 (13.2, 42.2)

* PCASP is available only on aircraft for HI-SCALE and ACE-ENA. UHSAS is available only in surface measurements for HI-SCALE and ACE-ENA, and in other field campaigns.

Both observed and simulated aerosol size distribution and number concentration show large variability during these field campaigns. Over the period of a few weeks or longer, aerosol number can vary by an order of magnitude between the 10% and 90% percentiles, especially for small particles (Figure 5). Figure 6 shows mean aerosol size distributions for two flight days during HI-SCALE: one with a large number of small (<70 nm) particles (14 May) and the other (3 September) with fewer small particles but more accumulation mode (70 – 300 nm) particles. On both days, EAMv1 reproduced the observed planetary boundary layer (PBL) height (PBLH) reasonably well with sufficient samples below and above PBL. On 14 May, EAMv1 reproduces the observed aerosol size distribution reasonably well both within the PBL and in the lower free atmosphere. However, on 3 September EAMv1 produces too many aerosols in the Aitken mode and too few accumulation mode aerosols in the PBL. In the free atmosphere, EAMv1 reproduces the lower concentration of Aitken mode aerosols but still underestimates the accumulation mode. Such contrasting cases will be useful to help diagnose the specific processes contributing to model uncertainties in future analyses. This large day-to-day variability also indicates that long-term measurements are needed to avoid sampling bias in building robust statistics in aerosol properties. The next version of ESMAC Diags will be extended to include the available long-term ARM measurements at SGP, ENA and other sites outside of the field campaign time periods.
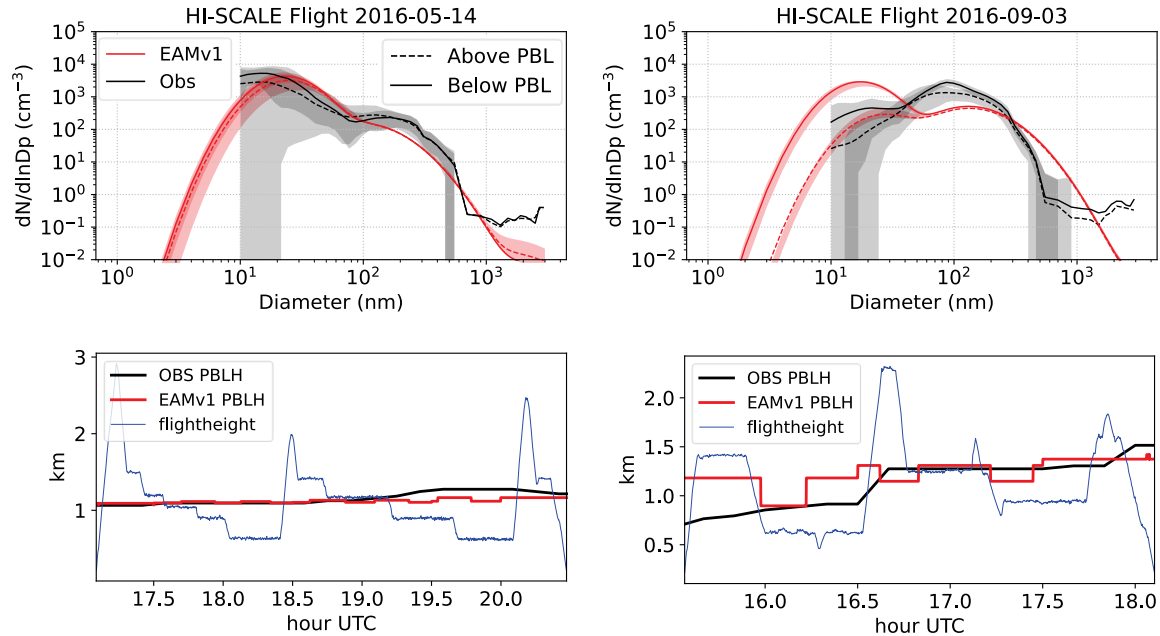
Figure 6: (Top) Mean aerosol number distribution for two flights during HI-SCALE: (left) 14 May 2016 and (right) 3 September 2016, for data above (dashed line) and below (solid line) observed PBLH. If there is cloud observed within a 1-hour window of the sample point, the above-PBL sample needs to be above cloud top and the below-PBL sample needs to be below cloud base for the sample point to be chosen. Shadings represent the data range between 10% and 90% percentiles. Relatively large particles with no shading indicate more than 90% of samples with zero values.

(bottom) Timeseries of observed (black) and simulated (red) PBLH overlaid with flight height (blue) during the two flight periods. The observed PBLH is derived from Doppler lidar measurements.

3.2 Vertical profiles of aerosol properties

A research aircraft is the primary platform to provide information on the vertical variations of key aerosol properties that cannot be obtained accurately by remote sensing instrumentation. In this section we show an example of evaluating vertical profiles of aerosol properties using aircraft measurements as well as illustrate the capability of evaluating multiple model simulations with ESMAC Diags. In addition to the standard EAMv1 simulation described in the previous section, we performed an EAMv1 simulation using the regionally refined mesh (RRM) (Tang et al., 2019). The model is configured to run with the horizontal grid spacing of ~0.25° over the continental U.S. and ~1° elsewhere. The two model configurations are identical, except for the higher spatial resolution (including primary aerosol emissions) in the RRM over

321   the continental U.S. All aircraft measurements with a cloud detected simultaneously (cloud flag = 1) were

322   excluded.

323   Figure 7 shows vertical percentiles of aerosol number concentration, composition and CCN number

324   concentration among all the HI-SCALE aircraft flights. Note that aircraft rarely flew above 3 km during

325   HI-SCALE so the sample size above that altitude is much smaller. All observed aerosol properties

326   decrease with height since the major sources of aerosols (anthropogenic, biogenic, and biomass burning)

327   (Liu et al., 2021) are from precursors emitted near the surface and chemical formation within the PBL.

328   EAMv1 generally simulates less variability than observations except for sulfate. Overall, EAMv1

329   reproduces the observed mean aerosol number concentration for aerosol size > 10 nm but underestimates

330   the number of larger particles > 100 nm during HI-SCALE (Table 3). The model also overestimates

331   sulfate and underestimates organic matter concentrations when compared to aircraft AMS measurements.

332   Its underestimation of CCN number concentration is consistent with underestimation of aerosol number

333   concentration for diameter > 100 nm but contrary with overestimation of sulfate. A similar relationship is

334   seen for ACE-ENA, to be described later in this section.
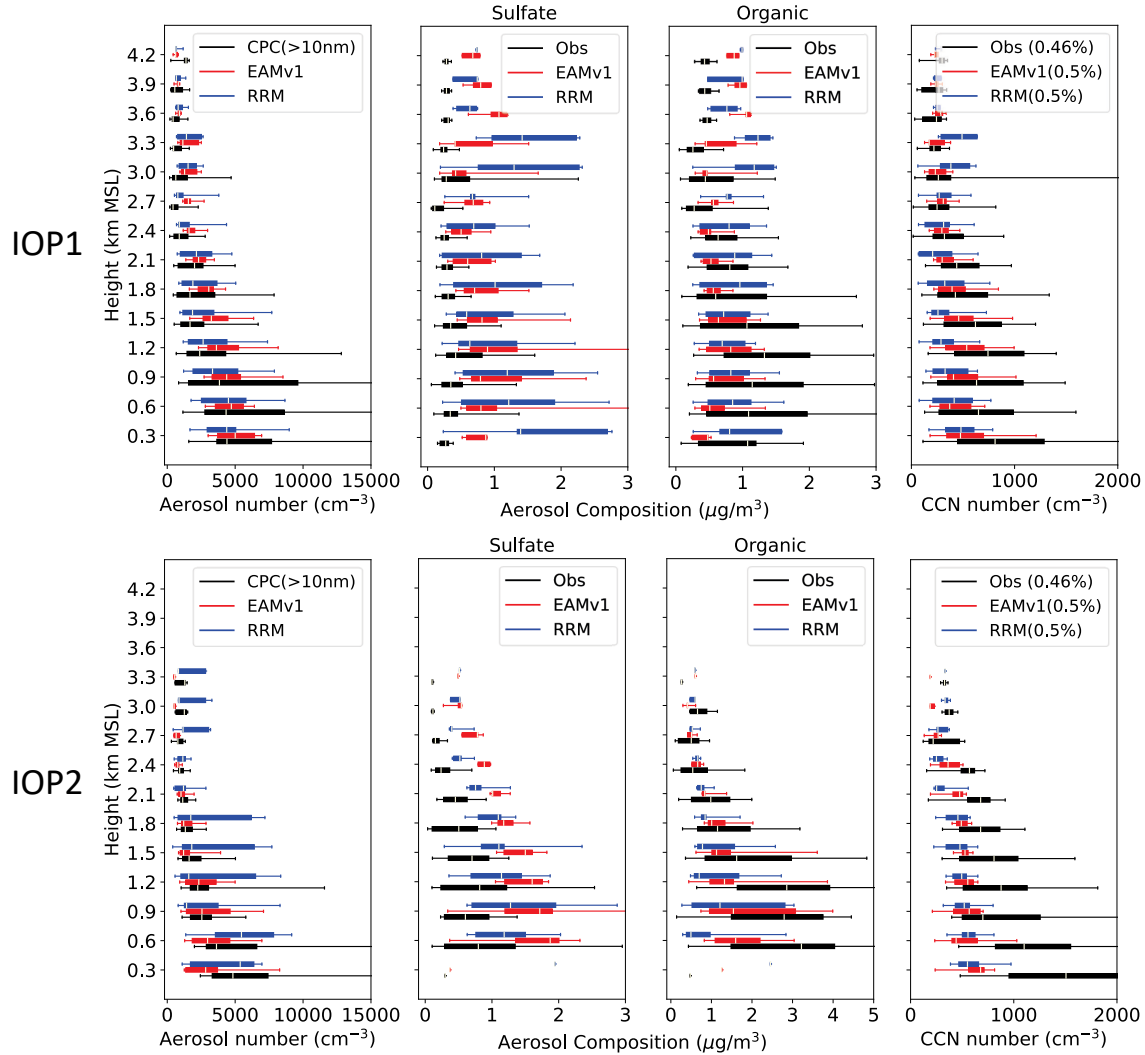
Figure 7: Vertical profiles of (from left to right): aerosol number concentration, mass concentration of sulfate, mass concentration of total organic matter and CCN number concentration under the supersaturation in the parentheses for HI-SCALE (top) IOP1 and (bottom) IOP2. The percentile box represents 25% and 75% percentiles, and the bar represents 5% and 95% percentiles.

The differences in sulfate and organic matter aloft is consistent with longer term surface measurement differences shown in Figure 8, suggesting this is a model bias. Note that near-surface measurements by aircraft are not always consistent with ground measurements (e.g., total organic matter in IOP1), which reflects the large spatial variability in aerosol properties associated with the aircraft flight paths up to a few hundred kilometers around the ARM site. The greater fraction of sulfate in EAMv1 suggests that the simulated aerosol hygroscopicity is likely higher than observed. Currently only these two species are available in both EAMv1 and AMS/ACSM observations for comparison purpose. Zaveri et al. (2021)

348   recently added chemistry associated with NO₃ formation in MAM4, which is expected to be implemented

349   in a future version of EAM.
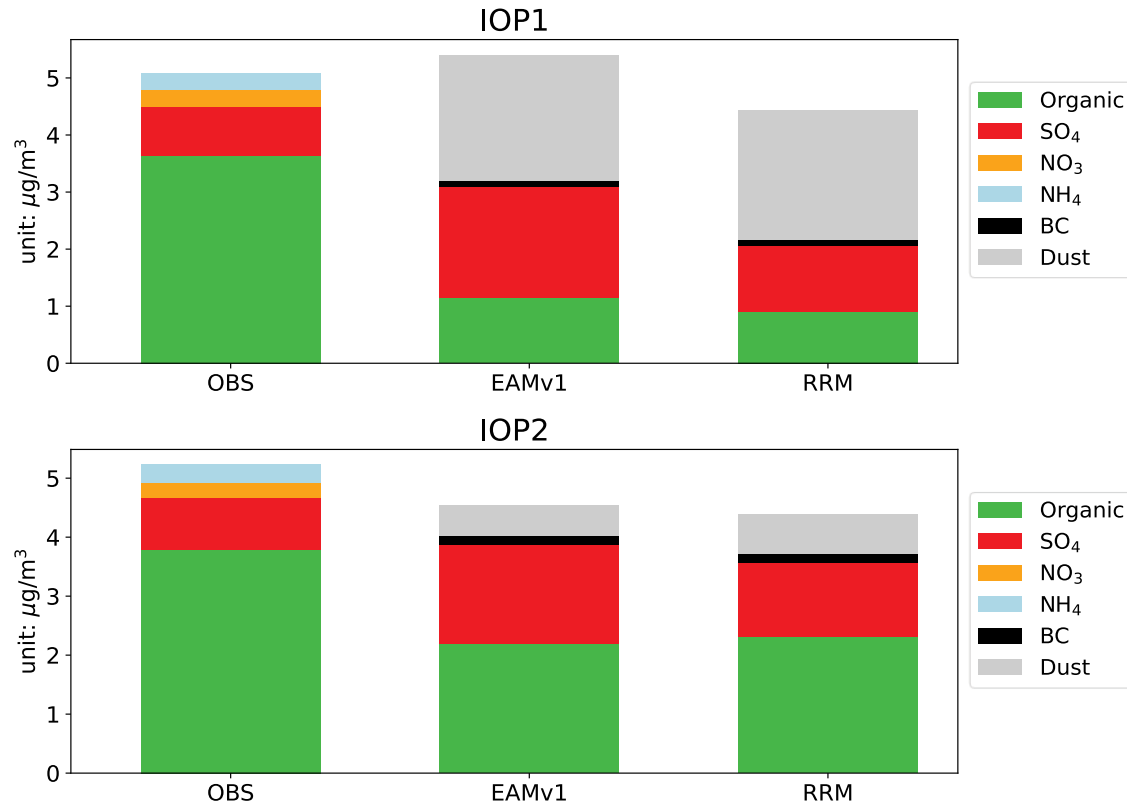
351   **Figure 8: Bar plots of the surface average aerosol composition during HI-SCALE IOP1 (top) and**

352   **IOP2 (bottom). Observations are obtained from an ACSM. Dust and black carbon (BC) are not**

353   **measured in the observation. NO₃ and NH₄ are not predicted in EAMv1 and RRM.**

354   Ongoing developments in E3SM will soon permit regional-refined meshes with grid spacings as small

355   as ~ 3 km as well as global convection-permitting simulations ($\Delta x \sim 3$ km); therefore, this diagnostics

356   package is designed to be flexible in scale to take advantage of higher-resolution ESM simulations that

357   are more compatible with high-resolution in-situ aerosol observations. This study demonstrates this

358   ability by using a 0.25° RRM simulation. Overall, the RRM analyzed here has similar biases as EAMv1,

359   with differences that vary seasonally. The 25% to 75% percentiles in Figure 7 show that the variability of

360   organic aerosols and CCN from the EAMv1 and RRM simulations are similar. However, the variability of

361   sulfate in RRM is larger than EAMv1 and observations during the spring IOP (IOP1). During the summer

362   IOP (IOP2), the variabilities of sulfate in EAMv1, RRM, and observations are similar, and the sulfate

363   concentrations from RRM are closer to observed than EAMv1. Individual timeseries from the RRM

364   simulation are still too smooth to capture the fine scale variability of aerosols in observations (not shown).

365 We expect E3SM to capture more fine scale variabilities related to urban and point sources of aerosols
366 and their precursors when the simulation grid spacing is further reduced to ~ 3 km. A sensitivity study
367 will be conducted when this high-resolution version of E3SM simulation becomes available.

368 Figure 9 shows the vertical variation in percentiles of aerosol properties for ACE-ENA. The observed
369 aerosol number concentrations, composition masses, and CCN number concentrations are much smaller
370 than those for HI-SCALE, representing a cleaner ocean environment. EAMv1 produces larger mean
371 values than the observations for all these quantities. The overall variabilities in predicted aerosol number
372 and concentrations of sulfate and organic matter are also greater than observed. Note that the observed
373 variabilities for HI-SCALE are much larger than for ACE-ENA, indicating that EAMv1 has smaller
374 location variation on aerosol variabilities. The observed total organic concentration shows a peak aloft
375 between 1.6 and 2.2 km, corresponding to the level of CCN number concentration peak. This implies a
376 major source of aerosols or precursors is free tropospheric transport (Zawadowicz et al., 2021). This peak
377 of total organic concentration aloft is also captured by the model.

378 The bar plots in Figure 10 of aerosol composition at the surface during ACE-ENA from the ACSM
379 instrument and EAMv1 illustrate a similar bias in sulfate and organic mass as aloft. While the surface
380 sulfate measurements are like those from the aircraft at the lowest altitudes, the observed surface organic
381 matter is much higher than aloft, particularly during IOP2. The differences in these measurements may be
382 due to local effects or possible contamination from aircraft since the surface station is located near an
383 airport on an island.

384

385
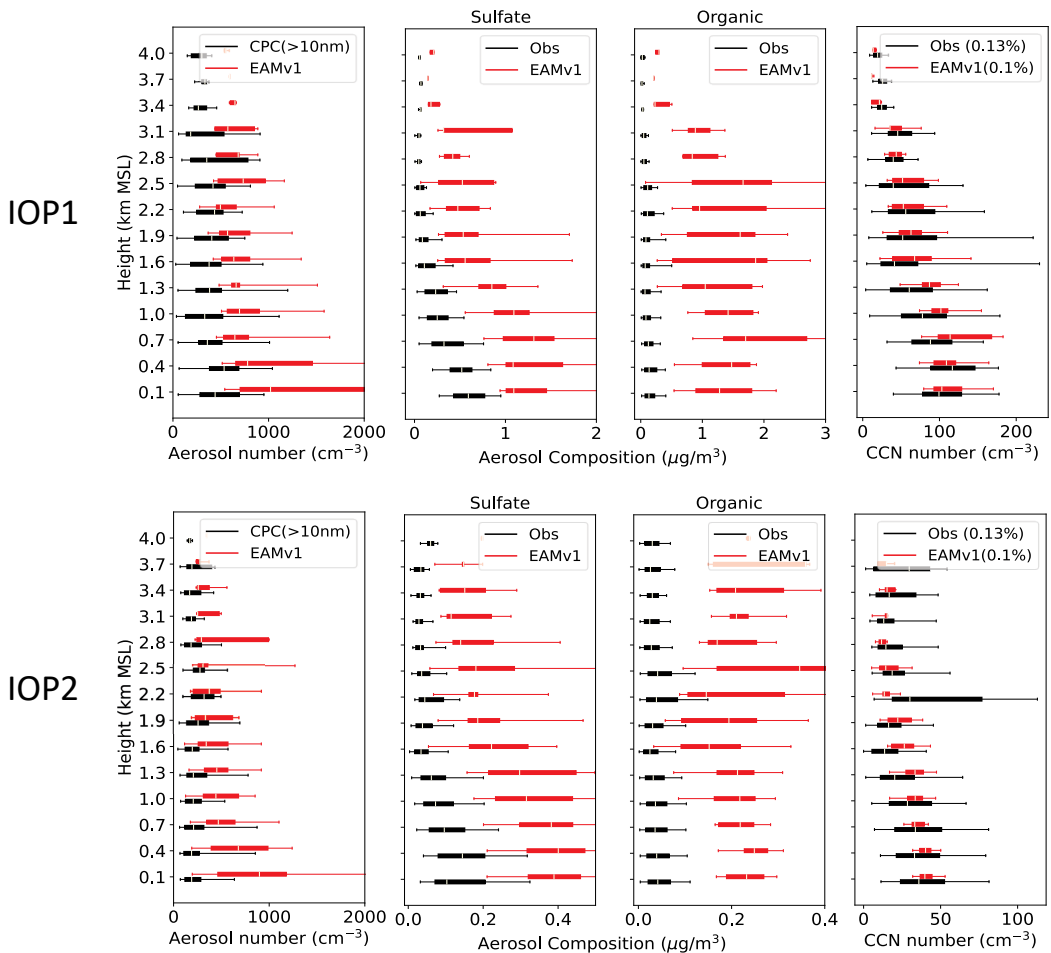
386   **Figure 9: Same as Figure 7 but for ACE-ENA.**

387
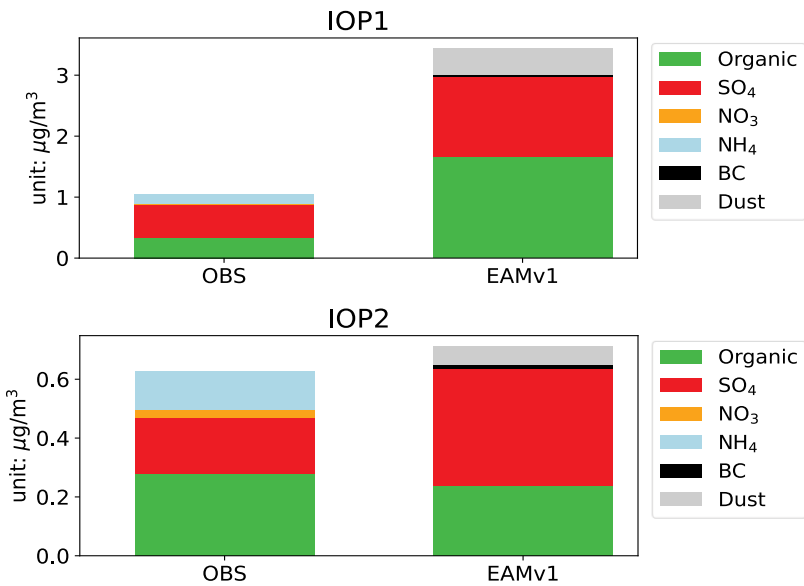
388   **Figure 10: Same as Figure 8 but for ACE-ENA.**

        ### 3.3 New particle formation events

390   Aerosol number concentrations and size distributions are highly impacted by NPF events (Kulmala et al.,

391   2004), which further influence CCN concentration (e.g., Kuang et al., 2009; Pierce and Adams, 2009) and

392   ultimately cloud properties. NPF and subsequent particle growth are frequently observed in the CUS

393   region (Hodshire et al., 2016). As described by Fast et al. (2019) and shown in Figure 11a, several NPF

394   events were observed during the HI-SCALE spring IOP (IOP1). Large concentrations of aerosols smaller

395   than 10 nm were observed, with the size growing larger over the next few hours. The average diurnal

396   variation in aerosol number distribution in Figure 12a shows that NPF events usually occur during the

397   morning between 12 and 15 UTC (6 – 9 am local time), followed by particle growth during the rest of the

398   morning and afternoon. This variation is also seen in the diurnally averaged CPC measurements of

399   aerosol diameters > 3 nm and > 10 nm (Figure 12c) but diurnal changes in CCN number concentrations

400   (Figure 12d) are more modest.

401
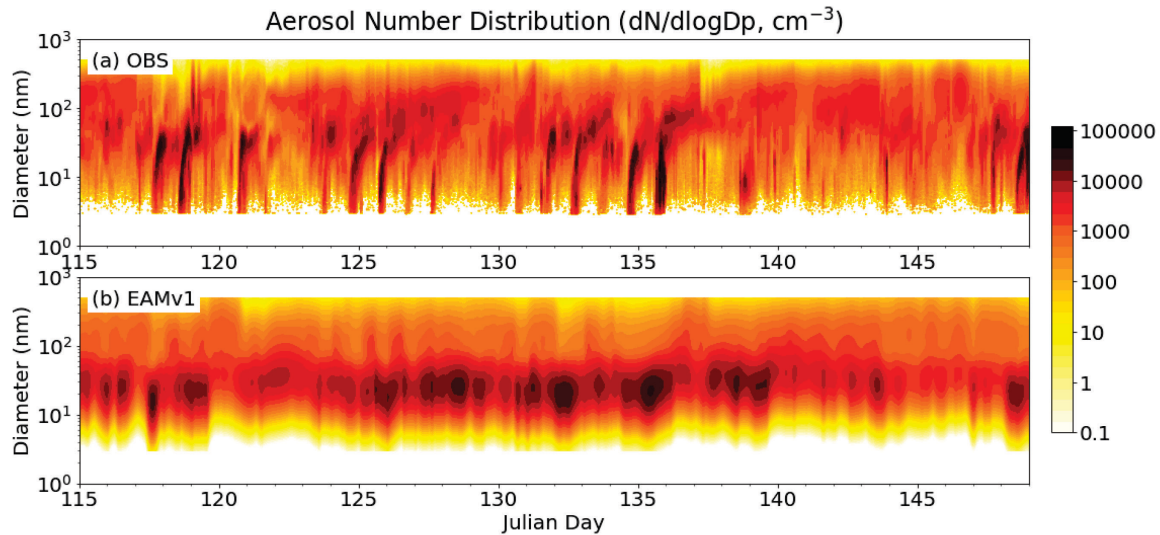
402   **Figure 11: Time series of (a) observed and (b) simulated surface aerosol number distribution**

403   **during HI-SCALE IOP1. The observed aerosol number distribution is from merged nanoSMPS**

404   **and SMPS. Model data is cut off at 500 nm to compare with observation.**
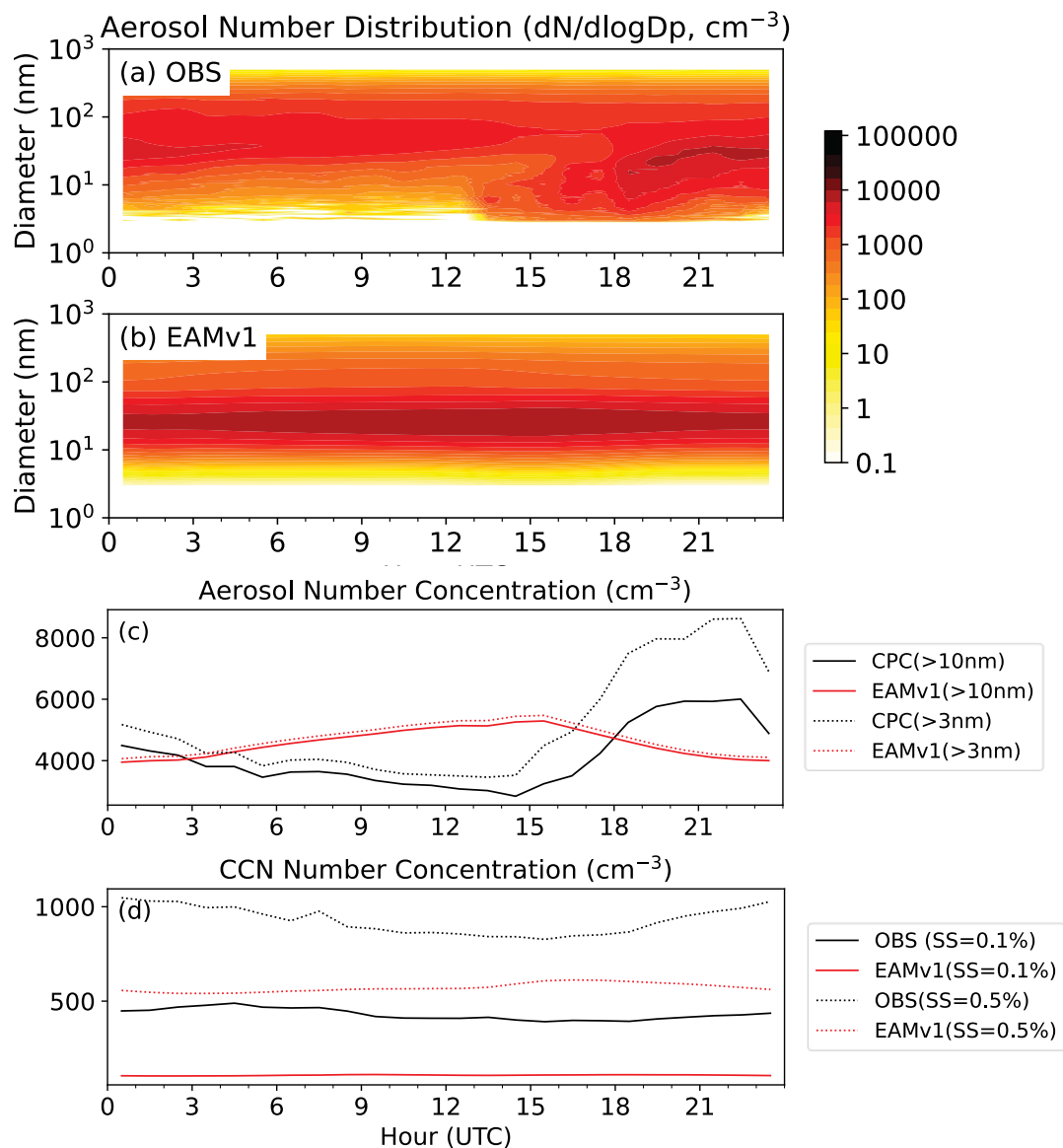
Figure 12: Average diurnal cycle of surface (a) observed aerosol number distribution, (b) simulated aerosol number distribution, (c) aerosol number concentration for diameters > 10 nm and > 3 nm, and (d) CCN number concentration for supersaturations of 0.1% and 0.5% for HI-SCALE IOP1.

Various NPF pathways associated with different chemical species have been proposed and implemented in models. Two NPF pathways are considered in MAM4 in EAMv1: a binary nucleation pathway and a PBL cluster nucleation pathway. However, the current simulation does not reproduce the observed large day-to-day variability of small particle concentrations due to NPF. Instead, the model produces high aerosol concentrations between 10 and 100 nm almost all the time. It also fails to reproduce

415   the large diurnal variability of aerosol and CCN number concentration with a peak seen in the morning

416   near 15 UTC (9 am local time), 7 hours earlier than the observed 22 UTC (4 pm local time) afternoon

417   peak. Its overestimation of aerosol number concentration for particle diameter >10 nm and

418   underestimation of CCN number concentration is consistent with that shown in Figure 5. Several efforts

419   are underway to improve the simulation of NPF by adding a nucleation mode in MAM4 to explicitly

420   resolve ultrafine particles and implementing new chemical pathways to simulate NPF following Zhao et

421   al. (2020). ESMAC Diags is being used to evaluate these new model developments.

422   Using aircraft measurements from ACE-ENA, Zheng et al. (2021) recently found evidence of NPF

423   events occurring in the upper part of marine boundary layer between broken clouds following the passage

424   of a cold front. 16 February 2018 is identified as a typical NPF day in Zheng et al. (2021). The vertical

425   profiles of aerosol number and CCN concentrations measured by aircraft on 16 February 2018 are shown

426   in Figure 13. The NPF event and particle growth happened in the upper boundary layer is shown by the

427   large mean and variance of aerosol number concentration just below the base of the marine boundary

428   layer clouds. EAMv1 could not simulate NPF events in the upper marine boundary layer on this day and

429   other days during ACE-ENA, likely due to the lack of NPF mechanisms related to dimethyl sulfide

430   (DMS) oxidation, and/or missing part in parameterizations to deal with the processes related to broken

431   marine boundary layer clouds and sub-grid circulation. Similarly, the sharp increase of CCN number just

432   above the level of marine boundary layer clouds is not simulated.

433
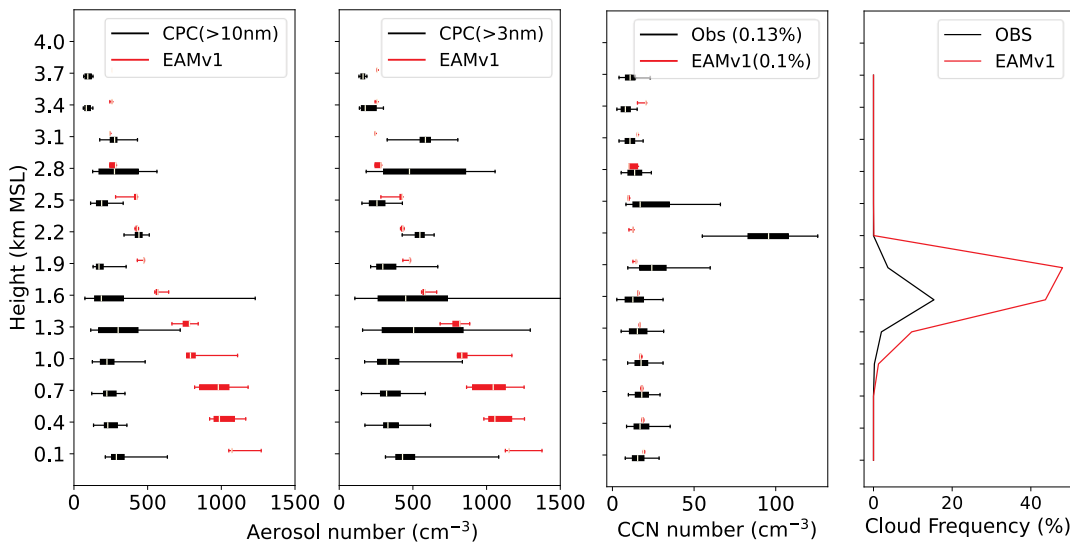
434   **Figure 13: Vertical profiles of aerosol number concentration for diameters >10 nm and >3 nm,**

435   **CCN number concentration, and cloud frequency measured by the 16 February 2018 flight in**

436   **ACE-ENA. The percentile box represents 25% and 75% percentiles, and the bar represents 5%**

437   **and 95% percentiles.**

438

3.4 Latitudinal dependence of aerosols and clouds

Unlike some field campaigns (i.e., HI-SCALE and ACE-ENA) where aircraft missions were conducted

over a relatively localized region with limited spatial variability of the meteorological conditions, ship

and/or aircraft measurements over the NEP and SO testbed regions span regions > 1500 km (i.e., from

California to Hawaii and from Tasmania to the far Southern Ocean, respectively). As shown in Figure 3,

there are large spatial gradients in EAMv1 simulated aerosol optical depth along these ship/aircraft tracks.

In ESMAC Diags version 1, we include composite plots of aerosol and cloud properties binned by

latitude to assess model representation of synoptic-scale variations.

447
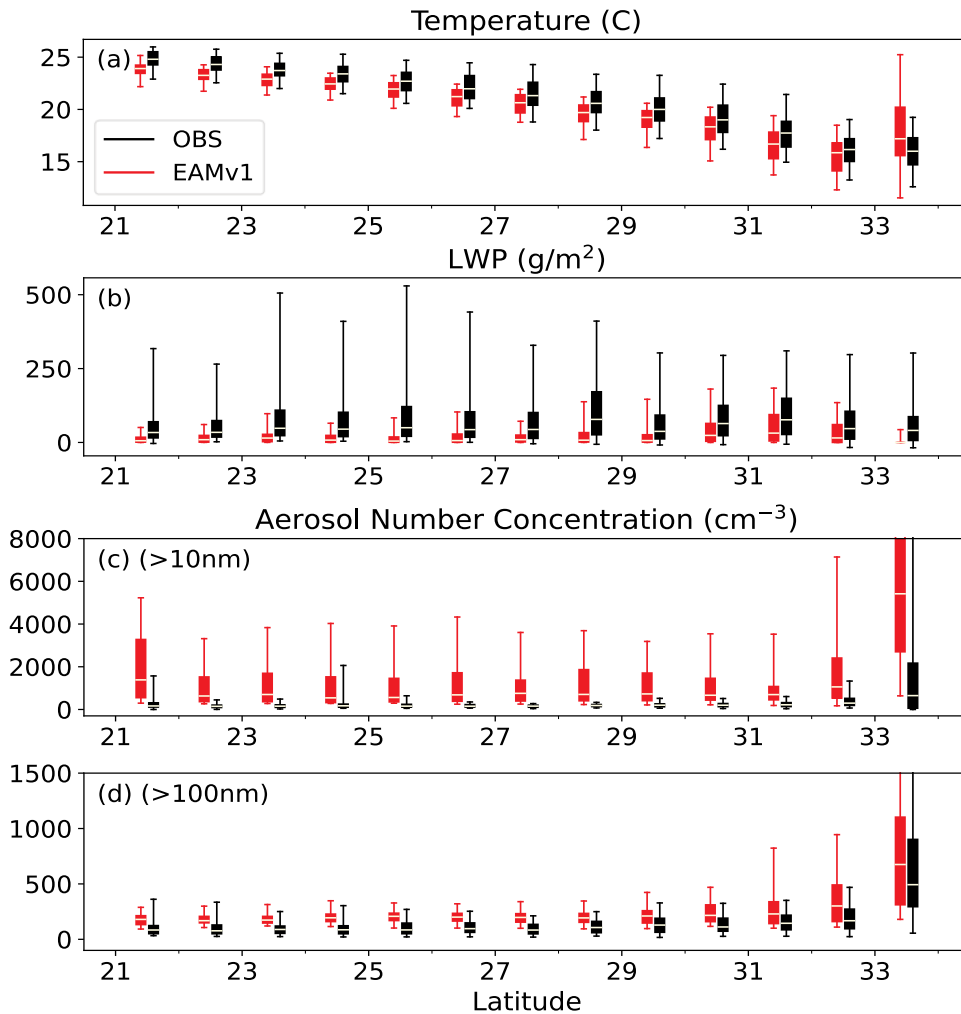
Figure 14: Percentiles of (a) air temperature, (b) grid-mean liquid water path (LWP), (c) aerosol

number concentration for diameter >10 nm, and (d) aerosol number concentration for

diameter >100 nm for all ship tracks in MAGIC binned by 1° latitude bins. The percentile box

451 **represents 25% and 75% percentiles, and the bar represents 5% and 95% percentiles. The**

452 **observed aerosol number concentrations for diameters >10 nm and >100 nm are obtained from**

453 **CPC and UHSAS, respectively.**

454

455
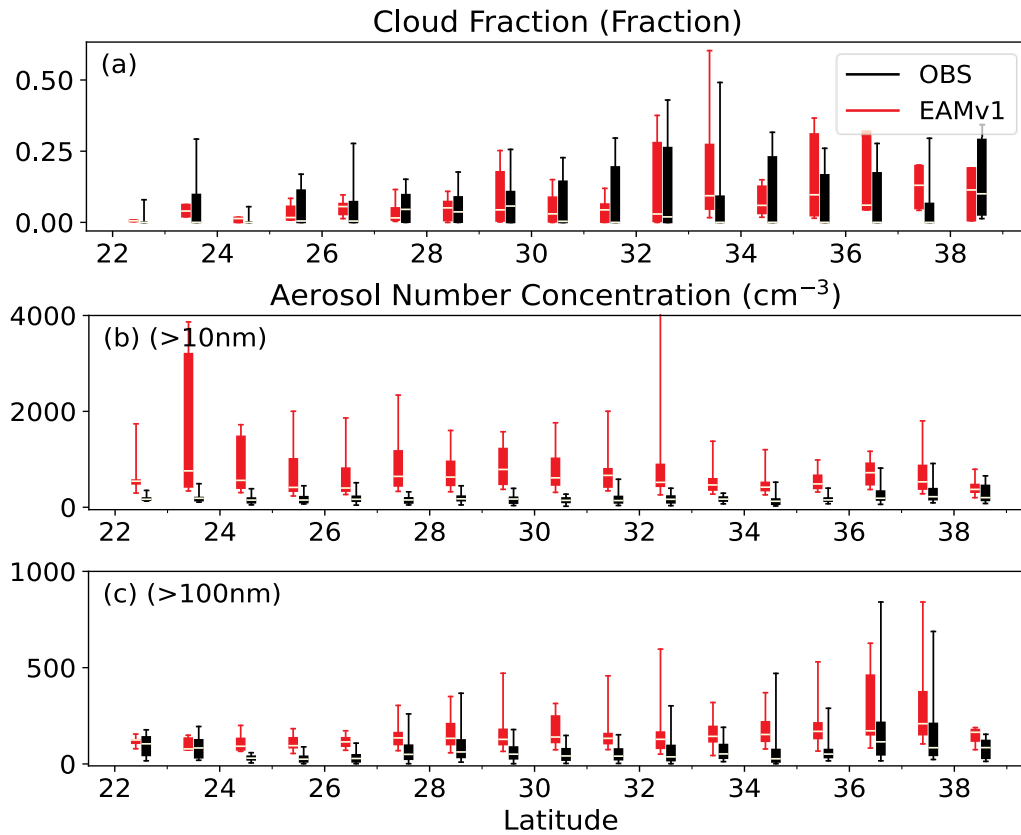
456 **Figure 15: Percentiles of (a) cloud fraction, (b) aerosol number concentration for diameter >10 nm,**

457 **and (c) aerosol number concentration for diameter >100 nm for all aircraft measurements between**

458 **0-3 km in CSET binned by 1° latitude bins. The percentile box represents 25% and 75%**

459 **percentiles, and the bar represents 5% and 95% percentiles. The observed aerosol number**

460 **concentrations for diameters >10 nm and >100 nm are obtained from CNC and UHSAS,**

461 **respectively.**

462

463   The research ship (aircraft) from the MAGIC (CSET) field campaign in the NEP testbed travelled

464 between California and Hawaii, where there is frequently a transition between marine stratocumulus

465 clouds near California and broken trade cumulus clouds near Hawaii (e.g., Teixeira et al., 2011).

466 Although ESMAC Diags v1 focuses primarily on aerosols, we show some basic meteorological and cloud

467   fields here since they are important to illustrate the transition of cloud regimes along the ship (aircraft)

468   tracks. Additional cloud properties derived from surface and satellite measurements are not included in

469   the current analysis, but are being implemented in ESMAC Diags v2. Some of the meteorological, cloud,

470   and aerosol properties along the ship (aircraft) tracks binned by latitude are shown in Figure 14 (Figure

471   15). Note that cloud fraction in Figure 15 is calculated as cloud frequency in aircraft observation and from

472   grid-mean cloud fraction in model along the flight track. This is different from the classic definition of

473   cloud fraction usually used for satellite measurements or models and is subject to aircraft sampling

474   strategy. As the surface temperature increases from California to Hawaii (Figure 14a), the cloud fraction

475   (Figure 15a) shows an decreasing trend southwestward, indicating the transition from stratocumulus to

476   cumulus clouds. However, ship-measured LWP (Figure 14b) has no trend related to latitude, possibly

477   because cumulus clouds at lower latitudes have smaller cloud fraction but larger LWP when clouds exist.

478   EAMv1 shows decreasing trends of both cloud fraction and LWP from high to low latitudes along these

479   tracks. It generally underestimates LWP and overestimates cloud fraction to the north of 30° N. For

480   aerosol number concentrations, EAMv1 produces too many aerosols compared to measurements both at

481   the surface (ship) and aloft (aircraft), consistent with the aerosol size distribution in Figure 5 and total

482   number concentration in Table 3. However, EAMv1 does reproduce the increase trend in accumulation

483   mode aerosol concentration approaching the California coast.

484   Similar latitudinal gradients of aerosol and CCN number concentrations along ship tracks from

485   MARCUS and aircraft tracks from SOCRATES are shown in Figures 16 and 17, respectively. Over the

486   SO region, NPF frequently occurs during austral summer when ample biogenic precursor gases (e.g.,

487   DMS) are released and rise into the free troposphere (McFarquhar et al., 2021; McCoy et al., 2021). Large

488   values of ship-measured aerosol and CCN number concentration are observed near Antarctica

489   corresponding to the coastal biological emissions of aerosol precursors, and also occur to the north of

490   45°S, indicating impacts from continental and anthropogenic sources. This is consistent with other studies

491   (Sanchez et al., 2021; Humphries et al., 2021). EAMv1 underestimates aerosol and CCN number

492   concentration near Antarctica. This bias, which may be related to too strong wet scavenging or

493   insufficient NPF and growth, is commonly seen in many other ESMs (e.g., McCoy et al., 2020; McCoy et

494   al., 2021). Aircraft flight paths during SOCRATES (Figure 17) do not extent as far south as the ship

495   measurements (Figure 16). The observed aerosol properties have little latitudinal variation in general.

496   EAMv1 underestimates aerosol number concentration for size > 10nm and CCN number concentration

497   with SS=0.5%, but the predictions are closer to observed for aerosol size > 100 nm and CCN with

498   SS=0.1% (Figure 17), consistent with the mean aerosol size distribution in Figure 5. This indicates that

499   the model performs better in simulating accumulation mode than Aitken mode particles over SO. These

500 model aerosol biases are highly relevant when considering their interaction with clouds and radiations,

501 which will be included in version 2 of ESMAC Diags.

502
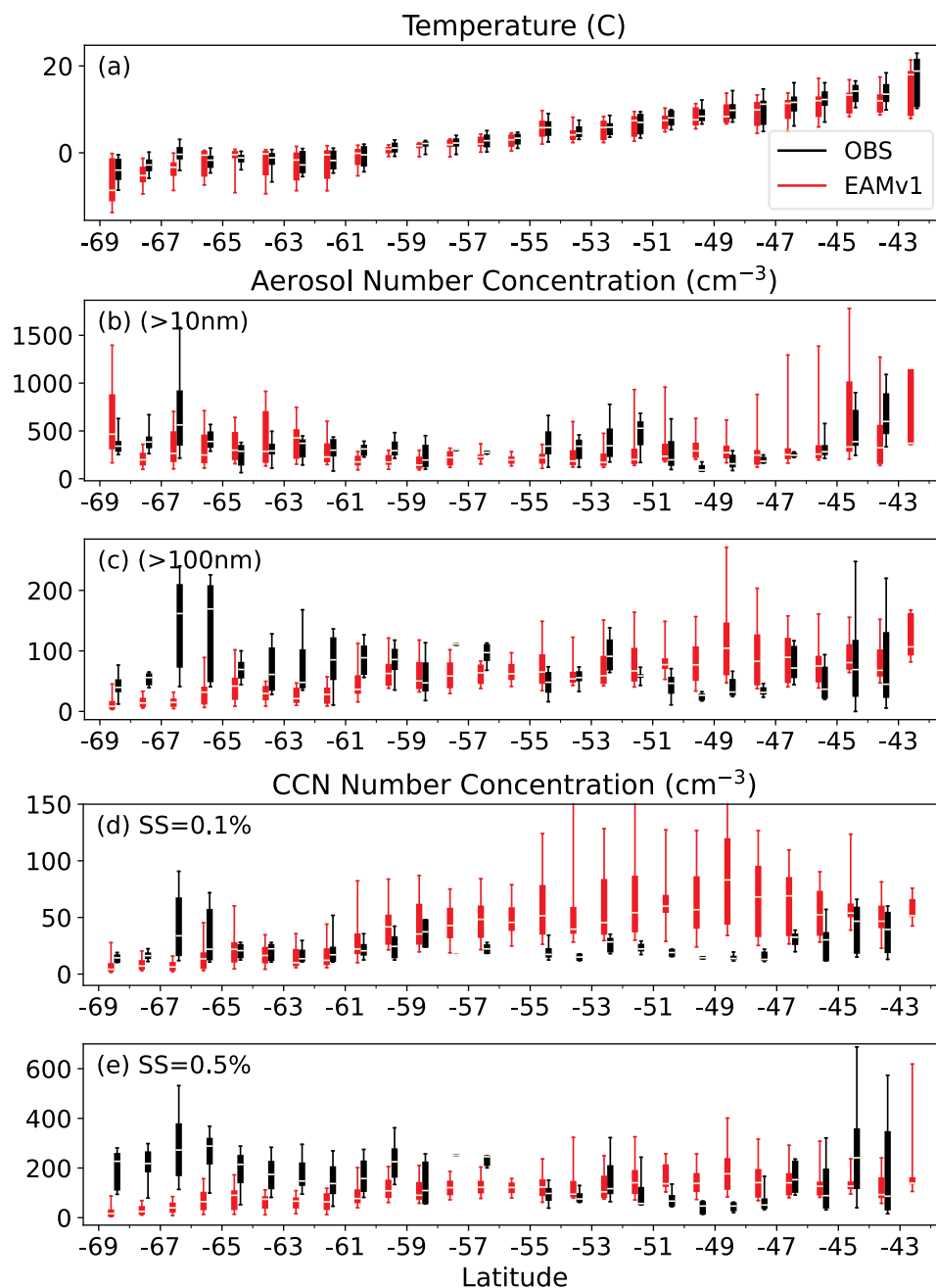
503

504 **Figure 16: Percentiles of (a) air temperature, (b) aerosol number concentration for diameter >10**

505 **nm, (c) aerosol number concentration for diameter >100 nm, (d) CCN number concentration for**

Figure 17: Percentiles of (a) aerosol number concentration for diameter >10 nm, (b) aerosol number concentration for diameter >100 nm, (c) CCN number concentration for supersaturation SS=0.1%, and (d) CCN number concentration for supersaturation SS=0.5% for all aircraft measurements between 0-3 km in SOCRATES binned by 1° latitude bins.

4. **Summary**

516 A Python-based ESM aerosol-cloud diagnostics (ESMAC Diags) package is developed to quantify the

517 performance of the DOE's E3SM atmospheric model using ARM and NCAR field campaign

518 measurements. The first version of this diagnostics package focuses on aerosol properties. The

519 measurements include aerosol number, size distribution, chemical composition, and CCN collected from

520 surface, aircraft, and ship platforms needed to assess how well the aerosol lifecycle is represented across

521 spatial and temporal scales which will subsequently impact uncertainties in aerosol radiative forcing

522 estimates. Currently, the diagnostics cover the field campaigns of ACE-ENA, HI-SCALE,

523 MAGIC/CSET, and MARCUS/SOCRATES over Northeastern Atlantic, Continental U.S., Northeastern

524 Pacific, and Southern Ocean, respectively. The code structure is designed to be flexible and modular so

525 that evaluation against new field campaigns or additional datasets can be easily implemented. Since there

526 is no one instrument that can measure the entire aerosol size distribution, we have constructed merged

527 aerosol size distributions from two or more ARM instruments to better assess predicted size distributions.

528 An "aircraft simulator" is used to extract aerosol and meteorological model variables along flight paths

529 that vary in space and time. Similarly, the aircraft simulator is applied to ship tracks in which the altitude

530 remains fixed at sea level.

531 The version 1 of ESMAC Diags package can provide various types of diagnostics and metrics,

532 including timeseries, diurnal cycles, mean aerosol size distribution, pie charts for aerosol composition,

533 percentiles by height, percentiles by latitude, mean statistics of aerosol number concentration, and more.

534 A full set of diagnostics plots and metrics for simulations used in this paper are available at

535 https://portal.nersc.gov/project/m3525/sqtang/ESMAC_Diags_v1/forGMD/webpage/. This allows

536 quantification of model performance predicting aerosol number, size, composition, vertical distribution,

537 spatial distribution (along ship tracks or aircraft tracks) and new particle formation events. This paper

538 shows some examples to demonstrate the capability of ESMAC Diags to evaluate EAMv1 simulated

539 aerosol properties. The diagnostics package also allows multiple simulations in one plot to compare

540 different models or model versions. It can also be applied to evaluate other ESMs with small

541 modifications to process model output.

542 Because in-situ aerosol measurements are usually collected at high temporal frequency (typically 1

543 second to a minute) over fine spatial volumes, there is a spatiotemporal scale mismatch with the standard

544 climate model resolution (usually 1-degree grid spacing with hourly output). This is a limitation that

545 cannot be completely overcome and must be accepted to perform model-observation comparisons

546 necessary for identifying shortcomings in model representation of aerosol, cloud, and aerosol-cloud

547 interaction processes that are the primary source for uncertainties in prediction of future climate. As new

548 versions of E3SM become available that has grid spacings as small as a few kilometers via regional-

549 refined and convection-permitting global domains (e.g., Caldwell et al., 2021), spatiotemporal

550 variabilities of aerosols at finer scales should be captured and be more compatible with fine resolution

551 observations such that resolution impacts on statistical differences can be quantified. The diagnostics

552 package will be applied to diagnose high resolution model output when the data are available.

553   While the current version focuses on aerosol properties, a version 2 of ESMAC Diags is being

554 developed to include more diagnostics and metrics for cloud, precipitation, and radiation properties to

555 facilitate the evaluation of aerosol-cloud interactions. These include inversion strength, above cloud

556 relative humidity, cloud-surface coupling, cloud fraction, depth, LWP, optical depth, effective radius,

557 droplet number concentration, adiabaticity, and albedo, precipitation rate, and more. Long-term surface-

558 based and satellite retrievals will also be used to provide better statistics in model evaluation and to

559 address limitations related to data coverage and uncertainty. Analyses are being designed to quantify

560 relationships between these variables and relate them to effective radiative forcing, which will be used to

561 assess and improve model parameterizations.

562   While there are other efforts to develop model diagnostics packages, this diagnostics package provides

563 a unique capability for detailed evaluation of aerosol properties that are tightly connected with

564 parameterized processes. Together with other commonly used diagnostics packages such as the ARM

565 diagnostics package (Zhang et al., 2020), the DOE E3SM diagnostics package, and the PCMDI's metrics

566 package (Gleckler et al., 2016), we expect to better understand the strengths and weaknesses of E3SM or

567 other ESMs and provide insights into model deficiencies to guide future model development. This

568 includes studies that develop a better understanding of how various processes contribute to uncertainties

569 in aerosol number and composition predictions and subsequent representation of CCN and aerosol

570 radiative forcing estimates.

571

572 Appendix A: Namelist containing the variables and regions of E3SM hourly output over the six field

573 campaigns used in the E3SM run script in this study. Here *fincl4* defines output variables with the 4th

574 frequency (1 hr) and interval (24 per day) in *nhtfrq* and *mfilt*, respectively. *fincl4latlon* defines the latitude

575 and longitude range of *fincl4* output.

```
576  nhtfrq      = 0,-24,-3,-1
577  mfilt       = 1,1,8,24
578  …
579  fincl4      = 'PS',      !! dynamical fields
580              'U',       !! ..
581              'V',       !! ..
582              'T',       !! ..
```

```
583        'Q',        !! vapor (kg/kg)
584        'CLDLIQ',    !! cloud hydrometeors (kg/kg)
585        'CLDICE',    !! ..
586        'CLDTOT',
587        'NUMLIQ',    !! ..
588        'NUMICE',    !! ..
589        'PBLH',      !! PBL height
590        'LHFLX',     !! energy fluxes
591        'SHFLX',     !! ..
592        'FLNT',      !! ..
593        'FSNT',      !! ..
594        'FLNS',      !! ..
595        'FSNS',      !! ..
596        'TREFHT',    !! ..
597        'Z3',        !! geopotential height
598        'RELHUM',    !! relative humidity (RH)
599        'RHW',       !! RH with respect to water
600        'RHI',       !! RH with respect to ice
601        'CLOUD',     !! cloud fraction
602        'AWNI',      !! in-cloud values
603        'AWNC',      !! Average cloud water number conc (1/m3)
604        'CCN1',      !! CCN concentration at S=0.02% (#/cm3)
605        'CCN3',      !! CCN concentration at S=0.1% (#/cm3)
606        'CCN4',      !! CCN concentration at S=0.2% (#/cm3)
607        'CCN5',      !! CCN concentration at S=0.5% (#/cm3)
608        'AREI',      !! ..
609        'AREL',      !! ..
610        'PRECT',     !! precipitation
611        'PRECC',     !! ..
612        'PRECL',     !! ..
613        'FICE',      !! ice mass fraction
614        'IWC',       !! grid box average ice water content (kg/m3)
615        'LWC',       !! grid box average liquid water content (kg/m3)
616        'TGCLDLWP',  !! liquid water path (including convective clouds)
617        'TGCLDIWP',  !! ice water path (including convective clouds)
618        'AODVIS',    !! AOD
619        'DMS',       !!
620        'SO2',       !!
621        'H2SO4',     !!
622        'bc_a1',     !! aerosols mass (kg/kg)
623        'bc_a3',     !!
624        'bc_a4',     !!
625        'dst_a1',    !!
626        'dst_a3',    !!
627        'mom_a1',    !!
628        'mom_a2',    !!
629        'mom_a3',    !!
630        'mom_a4',    !!
```

```
631          'ncl_a1',    !!
632          'ncl_a2',    !!
633          'ncl_a3',    !!
634          'pom_a1',    !!
635          'pom_a3',    !!
636          'pom_a4',    !!
637          'so4_a1',    !!
638          'so4_a2',    !!
639          'so4_a3',    !!
640          'soa_a1',    !!
641          'soa_a2',    !!
642          'soa_a3',    !!
643          'num_a1',    !! aerosols number (#/kg)
644          'num_a2',    !!
645          'num_a3',    !!
646          'num_a4',    !!
647          'num_c1',    !! aerosols number (#/kg)
648          'num_c2',    !!
649          'num_c3',    !!
650          'num_c4',    !!
651          'dgnd_a01',  !! dry aerosol size
652          'dgnd_a02',  !! ..
653          'dgnd_a03',  !! ..
654          'dgnd_a04',  !! ..
655          'dgnw_a01',  !! wet aerosol size
656          'dgnw_a02',  !! ..
657          'dgnw_a03',  !! ..
658          'dgnw_a04',  !! ..
659          'EXTINCT',   !! Aerosol extinction (1/m)
660          'AODABS',    !! Aerosol absorption optical depth 550 nm
661          'ABSORB',    !! Aerosol absorption (1/m)
662 fincl4lonlat = '260e:265e_34n:39n',  ! SGP (~5x5 degs)
663          '330e:335e_37n:42n',  ! ENA
664          '202e:240e_19n:40n',  ! CSET
665          '202e:243e_20n:35n',  ! MAGIC
666          '60e:160e_42s:70s',   ! MARCUS
667          '133e:164e_42s:63s',  ! SOCRATES
```

Code availability:

The current version of ESMAC Diags is publicly available through GitHub (https://github.com/eagles-project/ESMAC_diags) under the new BSD license. The exact version (1.0.0-beta.2) of the code used to produce the results used in this paper is archived on Zenodo (https://doi.org/10.5281/zenodo.6371596).

Data availability:

Measurements from the HI-SCALE, ACE-ENA, MAGIC, and MARCUS campaigns as well as the SGP and ENA sites are supported by the DOE Atmospheric Radiation Measurement (ARM) user facility and available at https://adc.arm.gov/discovery/. Measurements from the CSET and SOCRATES campaigns are supported by National Science Foundation (NSF) and obtained from NCAR Earth Observing Laboratory at https://data.eol.ucar.edu/master_lists/generated/cset/ and https://data.eol.ucar.edu/master_lists/generated/socrates/, respectively. DOI numbers or references of individual instruments are given in Table 2. All the above observational data and preprocessed model data used to produce the results used in this paper is archived on Zenodo (https://doi.org/10.5281/zenodo.6369120).

Author contribution:

ST, JDF and PM designed the diagnostics package; ST wrote the code and performed the analysis; JES, FM and MAZ processed the field campaign data; KZ contributed to the model simulation; JCH and ACV contributed to the package design and setup; ST wrote the original manuscript; all authors reviewed and edited the manuscript.

Competing interests:

Po-Lun Ma is a Topical Editor of Geoscientific Model Development. Other authors declare that they have no conflict of interest.

Acknowledgements:

This study was supported by the Enabling Aerosol-cloud interactions at GLobal convection-permitting scalES (EAGLES) project (74358), funded by the U.S. Department of Energy, Office of Science, Office of Biological and Environmental Research, Earth System Model Development (ESMD) program area. We thank the numerous instrument mentors for providing the data. This research used resources of the National Energy Research Scientific Computing Center (NERSC), a U.S. Department of Energy Office of Science User Facility operated under Contract No. DE-AC02-05CH11231. Pacific Northwest National Laboratory (PNNL) is operated for DOE by Battelle Memorial Institute under contract DE-AC05-76RL01830.

References:

699 **References**:

700 Albrecht, B., Ghate, V., Mohrmann, J., Wood, R., Zuidema, P., Bretherton, C., Schwartz, C., Eloranta, E.,
701 Glienke, S., Donaher, S., Sarkar, M., McGibbon, J., Nugent, A. D., Shaw, R. A., Fugal, J., Minnis, P.,
702 Paliknoda, R., Lussier, L., Jensen, J., Vivekanandan, J., Ellis, S., Tsai, P., Rilling, R., Haggerty, J., Campos,
703 T., Stell, M., Reeves, M., Beaton, S., Allison, J., Stossmeister, G., Hall, S., and Schmidt, S.: Cloud System
704 Evolution in the Trades (CSET): Following the Evolution of Boundary Layer Cloud Systems with the NSF–
705 NCAR GV, Bull. Amer. Meteor. Soc., 100, 93-121, https://doi.org/10.1175/bams-d-17-0180.1, 2019.

706 Albrecht, B. A.: Aerosols, Cloud Microphysics, and Fractional Cloudiness, Science, 245, 1227-1230,
707 https://doi.org/10.1126/science.245.4923.1227, 1989.

708 AMWG Diagnostic Package: https://www.cesm.ucar.edu/working_groups/Atmosphere/amwg-
709 diagnostics-package/, last access: 2 November 2021. 2021.

710 ARM Intensive Operational Period (IOP) Data Browser: https://iop.archive.arm.gov/arm-
711 iop/2012/mag/magic/reynolds-marmet/, last access: 2 November 2021. 2014.

712 ARM Intensive Operational Period (IOP) Data Browser: https://iop.archive.arm.gov/arm-
713 iop/2016/sgp/hiscale/tomlinson-pcasp, last access: 2 November 2021. 2016a.

714 ARM Intensive Operational Period (IOP) Data Browser: https://iop.archive.arm.gov/arm-
715 iop/2016/sgp/hiscale/mei-cpc, last access: 16 September 2021. 2016b.

716 ARM Intensive Operational Period (IOP) Data Browser: https://iop.archive.arm.gov/arm-
717 iop/2016/sgp/hiscale/wang-fims, last access: 2 November 2021. 2017.

718 ARM Intensive Operational Period (IOP) Data Browser: https://iop.archive.arm.gov/arm-
719 iop/2017/ena/aceena/mei-iwg1, last access: 2 November 2021. 2018.

720 ARM Intensive Operational Period (IOP) Data Browser: https://iop.archive.arm.gov/arm-
721 iop/2017/ena/aceena/wang-fims/, last access: 2 November 2021. 2020.

722 Caldwell, P. M., Terai, C. R., Hillman, B., Keen, N. D., Bogenschutz, P., Lin, W., Beydoun, H., Taylor,
723 M., Bertagna, L., Bradley, A. M., Clevenger, T. C., Donahue, A. S., Eldred, C., Foucar, J., Golaz, J.-C.,
724 Guba, O., Jacob, R., Johnson, J., Krishna, J., Liu, W., Pressel, K., Salinger, A. G., Singh, B., Steyer, A.,
725 Ullrich, P., Wu, D., Yuan, X., Shpund, J., Ma, H.-Y., and Zender, C. S.: Convection-Permitting Simulations
726 With the E3SM Global Atmosphere Model, Journal of Advances in Modeling Earth Systems, 13,
727 e2021MS002544, https://doi.org/https://doi.org/10.1029/2021MS002544, 2021.

728 Campbell, J. R., Hlavka, D. L., Welton, E. J., Flynn, C. J., Turner, D. D., Spinhirne, J. D., Scott , V. S., III,
729 and Hwang, I. H.: Full-Time, Eye-Safe Cloud and Aerosol Lidar Observation at Atmospheric Radiation
730 Measurement Program Sites: Instruments and Data Processing, J. Atmos. Ocean. Technol., 19, 431-442,
731 https://doi.org/10.1175/1520-0426(2002)019<0431:FTESCA>2.0.CO;2, 2002.

732 Carslaw, K. S., Lee, L. A., Regayre, L. A., and Johnson, J. S.: Climate Models Are Uncertain, but We Can
733 Do Something About It, Eos, 99, https://doi.org/10.1029/2018EO093757, 2018.

734 E3SM Diagnostics: https://e3sm.org/resources/tools/diagnostic-tools/e3sm-diagnostics/, last access: 2
735 November 2021. 2021.

736 Eyring, V., Righi, M., Lauer, A., Evaldsson, M., Wenzel, S., Jones, C., Anav, A., Andrews, O., Cionni, I.,
737 Davin, E. L., Deser, C., Ehbrecht, C., Friedlingstein, P., Gleckler, P., Gottschaldt, K. D., Hagemann, S.,
738 Juckes, M., Kindermann, S., Krasting, J., Kunert, D., Levine, R., Loew, A., Mäkelä, J., Martin, G., Mason,
739 E., Phillips, A. S., Read, S., Rio, C., Roehrig, R., Senftleben, D., Sterl, A., van Ulft, L. H., Walton, J., Wang,
740 S., and Williams, K. D.: ESMValTool (v1.0) – a community diagnostic and performance metrics tool for
741 routine evaluation of Earth system models in CMIP, Geosci. Model Dev., 9, 1747-1802,
742 https://doi.org/10.5194/gmd-9-1747-2016, 2016.

743 Fast, J. D., Gustafson, W. I., Chapman, E. G., Easter, R. C., Rishel, J. P., Zaveri, R. A., Grell, G. A., and
744 Barth, M. C.: The Aerosol Modeling Testbed: A Community Tool to Objectively Evaluate Aerosol Process
745 Modules, Bull. Amer. Meteor. Soc., 92, 343-360, https://doi.org/10.1175/2010bams2868.1, 2011.

746 Fast, J. D., Berg, L. K., Alexander, L., Bell, D., D'Ambro, E., Hubbe, J., Kuang, C., Liu, J., Long, C.,
747 Matthews, A., Mei, F., Newsom, R., Pekour, M., Pinterich, T., Schmid, B., Schobesberger, S., Shilling, J.,
748 Smith, J. N., Springston, S., Suski, K., Thornton, J. A., Tomlinson, J., Wang, J., Xiao, H., and Zelenyuk,
749 A.: Overview of the HI-SCALE Field Campaign: A New Perspective on Shallow Convective Clouds, Bull.
750 Amer. Meteor. Soc., 100, 821-840, https://doi.org/10.1175/bams-d-18-0030.1, 2019.

751 Gates, W. L., Boyle, J. S., Covey, C., Dease, C. G., Doutriaux, C. M., Drach, R. S., Fiorino, M., Gleckler,
752 P. J., Hnilo, J. J., Marlais, S. M., Phillips, T. J., Potter, G. L., Santer, B. D., Sperber, K. R., Taylor, K. E.,
753 and Williams, D. N.: An Overview of the Results of the Atmospheric Model Intercomparison Project
754 (AMIP I), Bull. Amer. Meteor. Soc., 80, 29-56, https://doi.org/10.1175/1520-
755 0477(1999)080<0029:Aootro>2.0.Co;2, 1999.

756 Gelaro, R., McCarty, W., Suarez, M. J., Todling, R., Molod, A., Takacs, L., Randles, C., Darmenov, A.,
757 Bosilovich, M. G., Reichle, R., Wargan, K., Coy, L., Cullather, R., Draper, C., Akella, S., Buchard, V.,
758 Conaty, A., da Silva, A., Gu, W., Kim, G. K., Koster, R., Lucchesi, R., Merkova, D., Nielsen, J. E., Partyka,
759 G., Pawson, S., Putman, W., Rienecker, M., Schubert, S. D., Sienkiewicz, M., and Zhao, B.: The Modern-
760 Era Retrospective Analysis for Research and Applications, Version 2 (MERRA-2), J. Climate, 30, 5419-
761 5454, https://doi.org/10.1175/JCLI-D-16-0758.1, 2017.

762 Gleckler, P. J., Doutriaux, C., Durack, P. J., Taylor, K. E., Zhang, Y., Williams, D. N., Mason, E., and
763 Servonnat, J.: A more powerful reality test for climate models, Eos, Trans. Amer. Geophys. Union, 97,
764 https://doi.org/10.1029/2016EO051663, 2016.

765 Golaz, J.-C., Caldwell, P. M., Van Roekel, L. P., Petersen, M. R., Tang, Q., Wolfe, J. D., Abeshu, G.,
766 Anantharaj, V., Asay-Davis, X. S., Bader, D. C., Baldwin, S. A., Bisht, G., Bogenschutz, P. A., Branstetter,
767 M., Brunke, M. A., Brus, S. R., Burrows, S. M., Cameron-Smith, P. J., Donahue, A. S., Deakin, M., Easter,
768 R. C., Evans, K. J., Feng, Y., Flanner, M., Foucar, J. G., Fyke, J. G., Griffin, B. M., Hannay, C., Harrop, B.
769 E., Hoffman, M. J., Hunke, E. C., Jacob, R. L., Jacobsen, D. W., Jeffery, N., Jones, P. W., Keen, N. D.,
770 Klein, S. A., Larson, V. E., Leung, L. R., Li, H.-Y., Lin, W., Lipscomb, W. H., Ma, P.-L., Mahajan, S.,
771 Maltrud, M. E., Mametjanov, A., McClean, J. L., McCoy, R. B., Neale, R. B., Price, S. F., Qian, Y., Rasch,
772 P. J., Reeves Eyre, J. E. J., Riley, W. J., Ringler, T. D., Roberts, A. F., Roesler, E. L., Salinger, A. G.,
773 Shaheen, Z., Shi, X., Singh, B., Tang, J., Taylor, M. A., Thornton, P. E., Turner, A. K., Veneziani, M.,
774 Wan, H., Wang, H., Wang, S., Williams, D. N., Wolfram, P. J., Worley, P. H., Xie, S., Yang, Y., Yoon, J.-
775 H., Zelinka, M. D., Zender, C. S., Zeng, X., Zhang, C., Zhang, K., Zhang, Y., Zheng, X., Zhou, T., and
776 Zhu, Q.: The DOE E3SM Coupled Model Version 1: Overview and Evaluation at Standard Resolution, J.
777 Adv. Model. Earth Syst., 11, 2089-2129, https://doi.org/10.1029/2018ms001603, 2019.

778 Hodshire, A. L., Lawler, M. J., Zhao, J., Ortega, J., Jen, C., Yli-Juuti, T., Brewer, J. F., Kodros, J. K.,
779 Barsanti, K. C., Hanson, D. R., McMurry, P. H., Smith, J. N., and Pierce, J. R.: Multiple new-particle

780   growth pathways observed at the US DOE Southern Great Plains field site, Atmos. Chem. Phys., 16, 9321-
781   9348, https://doi.org/10.5194/acp-16-9321-2016, 2016.

782   Howie, J. and Kuang, C.: Scanning Mobility Particle Sizer (AOSSMPS) [dataset],
783   https://doi.org/10.5439/1476898, Accessed 14 January 2020.

784   Humphries, R. S., Keywood, M. D., Gribben, S., McRobert, I. M., Ward, J. P., Selleck, P., Taylor, S.,
785   Harnwell, J., Flynn, C., Kulkarni, G. R., Mace, G. G., Protat, A., Alexander, S. P., and McFarquhar, G.:
786   Southern Ocean latitudinal gradients of cloud condensation nuclei, Atmos. Chem. Phys., 21, 12757-12782,
787   https://doi.org/10.5194/acp-21-12757-2021, 2021.

788   IPCC, Stocker, T. F., Qin, D., Plattner, G.-K., Tignor, M., Allen, S. K., Boschung, J., Nauels, A., Xia, Y.,
789   Bex, V., and Midgley, P. M. (Eds.): Climate Change 2013: The Physical Science Basis. Contribution of
790   Working Group I to the Fifth Assessment Report of the Intergovernmental Panel on Climate Change,
791   Cambridge University Press, Cambridge, United Kingdom and New York, NY, USA, 1535 pp.,
792   https://doi.org/10.1017/CBO9781107415324, 2013.

793   Koontz, A. and Kuang, C.: Scanning mobility particle sizer (AOSNANOSMPS) [dataset],
794   https://doi.org/10.5439/1242975, Accessed 14 January 2020.

795   Koontz, A. and Uin, J.: Ultra-High Sensitivity Aerosol Spectrometer (AOSUHSAS) [dataset],
796   https://doi.org/10.5439/1333828, Accessed 3 February 2021.

797   Kuang, C., McMurry, P. H., and McCormick, A. V.: Determination of cloud condensation nuclei production
798   from measured new particle formation events, Geophys. Res. Lett., 36,
799   https://doi.org/10.1029/2009GL037584, 2009.

800   Kuang, C., Salwen, C., and Singh, A.: Condensation Particle Counter (AOSCPCF) [dataset],
801   https://doi.org/10.5439/1046184, Accessed 24 November 2020.

802   Kuang, C., Andrews, E., Salwen, C., and Singh, A.: Condensation Particle Counter (AOSCPC) [dataset],
803   https://doi.org/10.5439/1025152, Accessed 16 September 2020.

804   Kuang, C., Salwen, C., Boyer, M., and Singh, A.: Condensation Particle Counter (AOSCPCF1M) [dataset],
805   https://doi.org/10.5439/1418260, Accessed 3 February 2021.

806   Kulmala, M., Vehkamäki, H., Petäjä, T., Dal Maso, M., Lauri, A., Kerminen, V. M., Birmili, W., and
807   McMurry, P. H.: Formation and growth rates of ultrafine atmospheric particles: a review of observations,
808   J. Aerosol Sci., 35, 143-176, https://doi.org/10.1016/j.jaerosci.2003.10.003, 2004.

809   Kyrouac, J. and Shi, Y.: Surface Meteorological Instrumentation (MET) [dataset],
810   https://doi.org/10.5439/1786358, Accessed 11 November 2020.

811   Lewis, E. R. and Teixeira, J.: Dispelling clouds of uncertainty, Eos, Trans. Amer. Geophys. Union, 96,
812   https://doi.org/10.1029/2015eo031303, 2015.

813   Liu, J., Alexander, L., Fast, J. D., Lindenmaier, R., and Shilling, J. E.: Aerosol characteristics at the
814   Southern Great Plains site during the HI-SCALE campaign, Atmos. Chem. Phys., 21, 5101-5116,
815   https://doi.org/10.5194/acp-21-5101-2021, 2021.

Liu, X., Ma, P. L., Wang, H., Tilmes, S., Singh, B., Easter, R. C., Ghan, S. J., and Rasch, P. J.: Description and evaluation of a new four-mode version of the Modal Aerosol Module (MAM4) within version 5.3 of the Community Atmosphere Model, Geosci. Model Dev., 9, 505-522, https://doi.org/10.5194/gmd-9-505-2016, 2016.

Maloney, E. D., Gettelman, A., Ming, Y., Neelin, J. D., Barrie, D., Mariotti, A., Chen, C. C., Coleman, D. R. B., Kuo, Y.-H., Singh, B., Annamalai, H., Berg, A., Booth, J. F., Camargo, S. J., Dai, A., Gonzalez, A., Hafner, J., Jiang, X., Jing, X., Kim, D., Kumar, A., Moon, Y., Naud, C. M., Sobel, A. H., Suzuki, K., Wang, F., Wang, J., Wing, A. A., Xu, X., and Zhao, M.: Process-Oriented Evaluation of Climate and Weather Forecasting Models, Bull. Amer. Meteor. Soc., 100, 1665-1686, https://doi.org/10.1175/bams-d-18-0042.1, 2019.

McCoy, I. L., Bretherton, C. S., Wood, R., Twohy, C. H., Gettelman, A., Bardeen, C. G., and Toohey, D. W.: Influences of Recent Particle Formation on Southern Ocean Aerosol Variability and Low Cloud Properties, J. Geophys. Res. Atmos., 126, https://doi.org/10.1029/2020jd033529, 2021.

McCoy, I. L., McCoy, D. T., Wood, R., Regayre, L., Watson-Parris, D., Grosvenor, D. P., Mulcahy, J. P., Hu, Y., Bender, F. A.-M., Field, P. R., Carslaw, K. S., and Gordon, H.: The hemispheric contrast in cloud microphysical properties constrains aerosol forcing, Proceedings of the National Academy of Sciences, 117, 18998-19006, https://doi.org/doi:10.1073/pnas.1922502117, 2020.

McFarquhar, G. M., Bretherton, C. S., Marchand, R., Protat, A., DeMott, P. J., Alexander, S. P., Roberts, G. C., Twohy, C. H., Toohey, D., Siems, S., Huang, Y., Wood, R., Rauber, R. M., Lasher-Trapp, S., Jensen, J., Stith, J. L., Mace, J., Um, J., Järvinen, E., Schnaiter, M., Gettelman, A., Sanchez, K. J., McCluskey, C. S., Russell, L. M., McCoy, I. L., Atlas, R. L., Bardeen, C. G., Moore, K. A., Hill, T. C. J., Humphries, R. S., Keywood, M. D., Ristovski, Z., Cravigan, L., Schofield, R., Fairall, C., Mallet, M. D., Kreidenweis, S. M., Rainwater, B., D'Alessandro, J., Wang, Y., Wu, W., Saliba, G., Levin, E. J. T., Ding, S., Lang, F., Truong, S. C. H., Wolff, C., Haggerty, J., Harvey, M. J., Klekociuk, A. R., and McDonald, A.: Observations of Clouds, Aerosols, Precipitation, and Surface Radiation over the Southern Ocean: An Overview of CAPRICORN, MARCUS, MICRE, and SOCRATES, Bull. Amer. Meteor. Soc., 102, E894-E928, https://doi.org/10.1175/bams-d-20-0132.1, 2021.

Mei, F.: Condensation particle counter for ACEENA [dataset], https://doi.org/10.5439/1440985, Accessed 5 December 2020.

Müller, D., Hostetler, C. A., Ferrare, R. A., Burton, S. P., Chemyakin, E., Kolgotin, A., Hair, J. W., Cook, A. L., Harper, D. B., Rogers, R. R., Hare, R. W., Cleckner, C. S., Obland, M. D., Tomlinson, J., Berg, L. K., and Schmid, B.: Airborne Multiwavelength High Spectral Resolution Lidar (HSRL-2) observations during TCAP 2012: vertical profiles of optical and microphysical properties of a smoke/urban haze plume over the northeastern coast of the US, Atmos. Meas. Tech., 7, 3487-3496, https://doi.org/10.5194/amt-7-3487-2014, 2014.

Myhre, G., Samset, B. H., Schulz, M., Balkanski, Y., Bauer, S., Berntsen, T. K., Bian, H., Bellouin, N., Chin, M., Diehl, T., Easter, R. C., Feichter, J., Ghan, S. J., Hauglustaine, D., Iversen, T., Kinne, S., Kirkevåg, A., Lamarque, J. F., Lin, G., Liu, X., Lund, M. T., Luo, G., Ma, X., van Noije, T., Penner, J. E., Rasch, P. J., Ruiz, A., Seland, Ø., Skeie, R. B., Stier, P., Takemura, T., Tsigaridis, K., Wang, P., Wang, Z., Xu, L., Yu, H., Yu, F., Yoon, J. H., Zhang, K., Zhang, H., and Zhou, C.: Radiative forcing of the direct aerosol effect from AeroCom Phase II simulations, Atmos. Chem. Phys., 13, 1853-1877, https://doi.org/10.5194/acp-13-1853-2013, 2013.

NETCDF: Introduction and Overview: https://www.unidata.ucar.edu/software/netcdf/docs/index.html, last access: 2 November 2021. 2021.

Petters, M. D. and Kreidenweis, S. M.: A single parameter representation of hygroscopic growth and cloud condensation nucleus activity, Atmos. Chem. Phys., 7, 1961-1971, https://doi.org/10.5194/acp-7-1961-2007, 2007.

Pierce, J. R. and Adams, P. J.: Uncertainty in global CCN concentrations from uncertain aerosol nucleation and primary emission rates, Atmos. Chem. Phys., 9, 1339-1356, https://doi.org/10.5194/acp-9-1339-2009, 2009.

Rasch, P. J., Xie, S., Ma, P.-L., Lin, W., Wang, H., Tang, Q., Burrows, S. M., Caldwell, P., Zhang, K., Easter, R. C., Cameron-Smith, P., Singh, B., Wan, H., Golaz, J.-C., Harrop, B. E., Roesler, E., Bacmeister, J., Larson, V. E., Evans, K. J., Qian, Y., Taylor, M., Leung, L. R., Zhang, Y., Brent, L., Branstetter, M., Hannay, C., Mahajan, S., Mametjanov, A., Neale, R., Richter, J. H., Yoon, J.-H., Zender, C. S., Bader, D., Flanner, M., Foucar, J. G., Jacob, R., Keen, N., Klein, S. A., Liu, X., Salinger, A. G., Shrivastava, M., and Yang, Y.: An Overview of the Atmospheric Component of the Energy Exascale Earth System Model, J. Adv. Model. Earth Syst., 11, 2377-2411, https://doi.org/10.1029/2019ms001629, 2019.

Reddington, C. L., Carslaw, K. S., Stier, P., Schutgens, N., Coe, H., Liu, D., Allan, J., Browse, J., Pringle, K. J., Lee, L. A., Yoshioka, M., Johnson, J. S., Regayre, L. A., Spracklen, D. V., Mann, G. W., Clarke, A., Hermann, M., Henning, S., Wex, H., Kristensen, T. B., Leaitch, W. R., Pöschl, U., Rose, D., Andreae, M. O., Schmale, J., Kondo, Y., Oshima, N., Schwarz, J. P., Nenes, A., Anderson, B., Roberts, G. C., Snider, J. R., Leck, C., Quinn, P. K., Chi, X., Ding, A., Jimenez, J. L., and Zhang, Q.: The Global Aerosol Synthesis and Science Project (GASSP): Measurements and Modeling to Reduce Uncertainty, Bull. Amer. Meteor. Soc., 98, 1857-1877, https://doi.org/10.1175/bams-d-15-00317.1, 2017.

Sanchez, K. J., Roberts, G. C., Saliba, G., Russell, L. M., Twohy, C., Reeves, J. M., Humphries, R. S., Keywood, M. D., Ward, J. P., and McRobert, I. M.: Measurement report: Cloud processes and the transport of biological emissions affect southern ocean particle and cloud condensation nuclei concentrations, Atmos. Chem. Phys., 21, 3427-3446, https://doi.org/10.5194/acp-21-3427-2021, 2021.

Schulz, M., Textor, C., Kinne, S., Balkanski, Y., Bauer, S., Berntsen, T., Berglen, T., Boucher, O., Dentener, F., Guibert, S., Isaksen, I. S. A., Iversen, T., Koch, D., Kirkevåg, A., Liu, X., Montanaro, V., Myhre, G., Penner, J. E., Pitari, G., Reddy, S., Seland, Ø., Stier, P., and Takemura, T.: Radiative forcing by aerosols as derived from the AeroCom present-day and pre-industrial simulations, Atmos. Chem. Phys., 6, 5225-5246, https://doi.org/10.5194/acp-6-5225-2006, 2006.

Seinfeld, J. H., Bretherton, C., Carslaw, K. S., Coe, H., DeMott, P. J., Dunlea, E. J., Feingold, G., Ghan, S., Guenther, A. B., Kahn, R., Kraucunas, I., Kreidenweis, S. M., Molina, M. J., Nenes, A., Penner, J. E., Prather, K. A., Ramanathan, V., Ramaswamy, V., Rasch, P. J., Ravishankara, A. R., Rosenfeld, D., Stephens, G., and Wood, R.: Improving our fundamental understanding of the role of aerosol−cloud interactions in the climate system, Proc. Natl. Acad. Sci. U.S.A, 113, 5781-5790, https://doi.org/10.1073/pnas.1514043113, 2016.

Sun, J., Zhang, K., Wan, H., Ma, P.-L., Tang, Q., and Zhang, S.: Impact of Nudging Strategy on the Climate Representativeness and Hindcast Skill of Constrained EAMv1 Simulations, J. Adv. Model. Earth Syst., 11, 3911-3933, https://doi.org/10.1029/2019MS001831, 2019.

Tang, Q., Klein, S. A., Xie, S., Lin, W., Golaz, J. C., Roesler, E. L., Taylor, M. A., Rasch, P. J., Bader, D. C., Berg, L. K., Caldwell, P., Giangrande, S. E., Neale, R. B., Qian, Y., Riihimaki, L. D., Zender, C. S.,

Zhang, Y., and Zheng, X.: Regionally refined test bed in E3SM atmosphere model version 1 (EAMv1) and applications for high-resolution modeling, Geosci. Model Dev., 12, 2679-2706, https://doi.org/10.5194/gmd-12-2679-2019, 2019.

Teixeira, J., Cardoso, S., Bonazzola, M., Cole, J., DelGenio, A., DeMott, C., Franklin, C., Hannay, C., Jakob, C., Jiao, Y., Karlsson, J., Kitagawa, H., Köhler, M., Kuwano-Yoshida, A., LeDrian, C., Li, J., Lock, A., Miller, M. J., Marquet, P., Martins, J., Mechoso, C. R., Meijgaard, E. v., Meinke, I., Miranda, P. M. A., Mironov, D., Neggers, R., Pan, H. L., Randall, D. A., Rasch, P. J., Rockel, B., Rossow, W. B., Ritter, B., Siebesma, A. P., Soares, P. M. M., Turk, F. J., Vaillancourt, P. A., Von Engeln, A., and Zhao, M.: Tropical and Subtropical Cloud Transitions in Weather and Climate Prediction Models: The GCSS/WGNE Pacific Cross-Section Intercomparison (GPCI), J. Climate, 24, 5223-5256, https://doi.org/10.1175/2011jcli3672.1, 2011.

Twomey, S.: The Influence of Pollution on the Shortwave Albedo of Clouds, J. Atmos. Sci., 34, 1149-1152, https://doi.org/10.1175/1520-0469(1977)034<1149:TIOPOT>2.0.CO;2, 1977.

Uin, J., Senum, G., Koontz, A., and Flynn, C.: Ultra-High Sensitivity Aerosol Spectrometer (AOSUHSAS) [dataset], https://doi.org/10.5439/1409033, Accessed 24 November 2020.

Wang, H., Easter, R. C., Zhang, R., Ma, P.-L., Singh, B., Zhang, K., Ganguly, D., Rasch, P. J., Burrows, S. M., Ghan, S. J., Lou, S., Qian, Y., Yang, Y., Feng, Y., Flanner, M., Leung, R. L., Liu, X., Shrivastava, M., Sun, J., Tang, Q., Xie, S., and Yoon, J.-H.: Aerosols in the E3SM Version 1: New Developments and Their Impacts on Radiative Forcing, J. Adv. Model. Earth Syst., 12, e2019MS001851, https://doi.org/10.1029/2019ms001851, 2020.

Wang, J., Wood, R., Jensen, M. P., Chiu, J. C., Liu, Y., Lamer, K., Desai, N., Giangrande, S. E., Knopf, D. A., Kollias, P., Laskin, A., Liu, X., Lu, C., Mechem, D., Mei, F., Starzec, M., Tomlinson, J., Wang, Y., Yum, S. S., Zheng, G., Aiken, A. C., Azevedo, E. B., Blanchard, Y., China, S., Dong, X., Gallo, F., Gao, S., Ghate, V. P., Glienke, S., Goldberger, L., Hardin, J. C., Kuang, C., Luke, E. P., Matthews, A. A., Miller, M. A., Moffet, R., Pekour, M., Schmid, B., Sedlacek, A. J., Shaw, R. A., Shilling, J. E., Sullivan, A., Suski, K., Veghte, D. P., Weber, R., Wyant, M., Yeom, J., Zawadowicz, M., and Zhang, Z.: Aerosol and Cloud Experiments in the Eastern North Atlantic (ACE-ENA), Bull. Amer. Meteor. Soc., 1-51, https://doi.org/10.1175/bams-d-19-0220.1, 2021.

Watson-Parris, D., Schutgens, N., Reddington, C., Pringle, K. J., Liu, D., Allan, J. D., Coe, H., Carslaw, K. S., and Stier, P.: In situ constraints on the vertical distribution of global aerosol, Atmos. Chem. Phys., 19, 11765-11790, https://doi.org/10.5194/acp-19-11765-2019, 2019.

Winker, D. M., Vaughan, M. A., Omar, A., Hu, Y., Powell, K. A., Liu, Z., Hunt, W. H., and Young, S. A.: Overview of the CALIPSO Mission and CALIOP Data Processing Algorithms, J. Atmos. Ocean. Technol., 26, 2310-2323, https://doi.org/10.1175/2009jtecha1281.1, 2009.

Zaveri, R. A., Easter, R. C., Singh, B., Wang, H., Lu, Z., Tilmes, S., Emmons, L. K., Vitt, F., Zhang, R., Liu, X., Ghan, S. J., and Rasch, P. J.: Development and Evaluation of Chemistry-Aerosol-Climate Model CAM5-Chem-MAM7-MOSAIC: Global Atmospheric Distribution and Radiative Effects of Nitrate Aerosol, J. Adv. Model. Earth Syst., 13, e2020MS002346, https://doi.org/10.1029/2020MS002346, 2021.

Zawadowicz, M. A., Suski, K., Liu, J., Pekour, M., Fast, J., Mei, F., Sedlacek, A. J., Springston, S., Wang, Y., Zaveri, R. A., Wood, R., Wang, J., and Shilling, J. E.: Aircraft measurements of aerosol and trace gas chemistry in the eastern North Atlantic, Atmos. Chem. Phys., 21, 7983-8002, https://doi.org/10.5194/acp-21-7983-2021, 2021.

Zhang, C., Xie, S., Tao, C., Tang, S., Emmenegger, T., Neelin, J. D., Schiro, K. A., Lin, W., and Shaheen, Z.: The ARM Data-Oriented Metrics and Diagnostics Package for Climate Models: A New Tool for Evaluating Climate Models with Field Data, Bull. Amer. Meteor. Soc., 101, E1619-E1627, https://doi.org/10.1175/bams-d-19-0282.1, 2020.

Zhang, K., Wan, H., Liu, X., Ghan, S. J., Kooperman, G. J., Ma, P. L., Rasch, P. J., Neubauer, D., and Lohmann, U.: Technical Note: On the use of nudging for aerosol–climate model intercomparison studies, Atmos. Chem. Phys., 14, 8631-8645, https://doi.org/10.5194/acp-14-8631-2014, 2014.

Zhao, B., Shrivastava, M., Donahue, N. M., Gordon, H., Schervish, M., Shilling, J. E., Zaveri, R. A., Wang, J., Andreae, M. O., Zhao, C., Gaudet, B., Liu, Y., Fan, J., and Fast, J. D.: High concentration of ultrafine particles in the Amazon free troposphere produced by organic new particle formation, Proc. Natl. Acad. Sci. U. S. A., 117, 25344-25351, https://doi.org/10.1073/pnas.2006716117, 2020.

Zheng, G., Wang, Y., Wood, R., Jensen, M. P., Kuang, C., McCoy, I. L., Matthews, A., Mei, F., Tomlinson, J. M., Shilling, J. E., Zawadowicz, M. A., Crosbie, E., Moore, R., Ziemba, L., Andreae, M. O., and Wang, J.: New particle formation in the remote marine boundary layer, Nat. Commun., 12, 527, https://doi.org/10.1038/s41467-020-20773-1, 2021.

Zhou, X., Kollias, P., and Lewis, E. R.: Clouds, Precipitation, and Marine Boundary Layer Structure during the MAGIC Field Campaign, J. Climate, 28, 2420-2442, https://doi.org/10.1175/jcli-d-14-00320.1, 2015.